Scaling of turbulence intensities up to $\mathrm{Re}_\tau = 10^6$ with a resolvent-based quasilinear approximation

Nikolaos Skouloudis and Yongyun Hwang[*]
Department of Aeronautics, Imperial College London, SW7 2AZ, United Kingdom

(Received 7 September 2020; accepted 10 February 2021; published 3 March 2021)

A minimal form of quasilinear approximation (QLA), recently proposed with a stochastic forcing and proper orthogonal decomposition modes [Hwang and Ekchardt, J. Fluid Mech. **894**, A23 (2020)], has been extended by employing a resolvent framework. A particular effort is made to reach an extremely high Reynolds number by carefully controlling the approximation without loss of the general scaling properties in the spectra, while setting out the main limitations and accuracy of the proposed QLA with possibility of further improvement. The QLA is subsequently applied to turbulent channel flow up to $\mathrm{Re}_\tau = 10^6$ (Re_τ is the friction Reynolds number). While confirming that the logarithmic wall-normal dependence in streamwise and spanwise turbulence intensities robustly appears, it reveals some nontrivial difference from the scaling of the classical attached eddy model based on inviscid flow assumption. First, the spanwise wave number spectra do not show any clearly visible inverse-law behavior due to the viscous wall effect prevailing in a significant portion of the lower part of the logarithmic layer. Second, the near-wall peak streamwise and spanwise turbulence intensities are found to deviate from $\ln \mathrm{Re}_\tau$ scaling for $\mathrm{Re}_\tau \gtrsim 10^4$. Importantly, the near-wall streamwise turbulence intensity is inversely proportional to $1/U_{cl}^+$ (U_{cl}^+ is the inner-scaled channel centreline velocity), consistent with the scaling obtained from an asymptotic analysis of the Navier-Stokes equations [Monkewitz and Nagib, J. Fluid Mech. **783**, 474 (2015)]. The same behavior was also observed for the streamwise turbulence intensity in the logarithmic region, as was predicted with the asymptotic analysis. Finally, the streamwise turbulence intensity in the logarithmic region is found to become greater than the near-wall one at $\mathrm{Re}_\tau \simeq O(10^5)$. It is shown that this behavior originates from the near-wall spectra associated with large-scale inactive motions, the intensity of which gradually decays as $\mathrm{Re}_\tau \to \infty$.

DOI: 10.1103/PhysRevFluids.6.034602

I. INTRODUCTION

A. Scaling of turbulence statistics and attached eddy hypothesis

Over the past two decades, there has been a substantial amount of evidence that supports the attached eddy hypothesis of Townsend [1,2] and some of the main predictions using the related models [3,4] (see Ref. [5] for a recent review). Under the hypothesis that the logarithmic mean velocity would admit the self-similar energy-containing eddies with respect to the distance from the wall (see also Ref. [6] where its mathematical basis is given), he developed an idealized theoretical model predicting the wall-normal behavior of turbulence intensity in the inviscid limit. In particular, by superposing a general form of the second-order statistical moments of the self-similar eddies subject to constant Reynolds shear stress, he predicted that the streamwise and spanwise turbulence

[*]y.hwang@imperial.ac.uk

intensities would have a logarithmic wall-normal dependence, while the wall-normal one would be a constant. It has recently been confirmed with laboratory experiments and direct numerical simulations (DNS) that his seminal prediction is indeed a good first approximation of turbulence intensities in the logarithmic layer [7–11]. Furthermore, the existence of such self-similar energy-containing motions in the logarithmic layer has been repeatedly reported with various types of eddy-extraction techniques [12–20]. Finally, several different types of mathematical analysis of the Navier-Stokes equations have consistently revealed that the self-similarity with the distance from the wall is the central feature of the logarithmic layer, which fundamentally underpins the scaling of the mean, linear, and nonlinear dynamics [21–33].

While it has been evident that the attached eddy hypothesis would play a central role in describing the statistical behavior of wall-bounded turbulence at high Reynolds numbers, it is important to remember that the early attached eddy models are highly idealized with the inviscid assumption, thereby retaining some inherent limitations in their predictions. First, the theoretical predictions of turbulent statistics are often refined based on some conceptual sketches obtained from flow visualizations: for example, the double-cone vortex model [2] or the hairpin vortex model [3]. These models would perhaps benefit from the invariant solutions to the Navier-Stokes equations [28,31,32]. However, they are fundamentally incompatible with the linear superposition used in the early attached eddy models [2,3,34,35], given the nonlinear nature of the Navier-Stokes equations. Second, the early models use the asymptotic feature of the logarithmic layer for high Reynolds numbers (i.e., the constant Reynolds shear stress), which is valid only in an approximate manner. Therefore, the extent of the validity remains a topic of ongoing investigations [5]. This issue would be particularly important in the region relatively close to the wall [26], such as the mesolayer (lower half of logarithmic layer), where the effect of viscosity would be non-negligible [23,36,37].

From this perspective, it is worth mentioning that a recent experimental measurement [38] and a DNS-data-based asymptotic analysis of the Navier-Stokes equations [39] have presented some evidence that the predictions of the early attached models based on the idealized setting (i.e., inviscid flow assumption) may not be fully relevant to the data obtained at "finite" Reynolds numbers. Indeed, the measurement from CICLoPE [38] suggests that the near-wall peak intensity may begin to deviate from a logarithmic growth with Reynolds number for $\mathrm{Re}_\tau \gtrsim 10^4$ (Re_τ is the friction Reynolds number), which has been understood as important evidence supporting the predictions of the early attached eddy model [40]. This behavior was more precisely predicted by an asymptotic analysis built upon the existing DNS data of turbulent boundary layers [39]. In particular, this study showed that the streamwise turbulence intensity in the near-wall region is proportional to $A_\infty - B_\infty/U_\infty^+$, where A_∞ and B_∞ are constants and $U_\infty \sim \ln \mathrm{Re}_\tau$ (the superscript $+$ indicates normalization by the inner units, and U_∞ is the free stream velocity). Furthermore, it was proposed that the Townsend-Perry constant would also be a function of Reynolds number.

B. Minimal quasilinear approximation

A minimal quasilinear approximation (QLA) of the Navier-Stokes equations has recently been proposed [33]. The key feature of the QLA is that it maintains the platform of the original attached eddy model [2], but is designed to overcome some of the aforementioned limitations especially caused by the invisicd flow assumption using the linearized Navier-Stokes equations [33]. In this approach, the velocity is decomposed into a mean and fluctuations. All nonlinear terms in the mean equation are kept, while the self-interacting nonlinear terms in the fluctuations equations are modeled with an eddy viscosity and a stochastic forcing. Under the assumption that the mean is known (e.g., the log law or the empirical profile of Ref. [41]), the color of the stochastic forcing is determined self-consistently by solving an optimization problem which minimizes the difference between the Reynolds shear stresses from the mean and fluctuation equations (this approach will be referred to as the stochastic QLA henceforth). We note that, in the optimization process of the QLA, the linear nature of the fluctuation equations enables one to determine the color of the stochastic forcing through a linear superposition of the self-similar stochastic response modes from the logarithmic layer [22], the feature exactly identical to the Townsend's original attached eddy model [33]. The best results were obtained when considered with two leading proper orthogonal decomposition (POD) modes, which eliminate the artifact caused by the nonphysical stochastic forcing in the approximation. In this case, the resulting turbulence intensities and the energy spectra exhibit exactly the same qualitative behavior as DNS data [10] throughout the entire wall-normal domain, while reproducing the early theoretical predictions of the original attached eddy model within the logarithmic layer (i.e., logarithmic wall-normal dependence of streamwise and spanwise turbulence intensities).

Another key feature of the stochastic QLA is the "prediction" and/or "extrapolation" capability of the basic scaling behavior of turbulence intensity and spectra with minimal data (i.e., mean velocity). This is the main difference from the other previous data-driven approaches utilizing the linearized Navier-Stokes equations as the modeling template [24,42–47]. Indeed, the QLA qualitatively preserves all the basic scaling behaviors in the velocity spectra at the level of DNS, except the one for energy cascade [22] originating from the self-interacting nonlinear terms modeled phenomenologically: i.e., the law of the wall and the velocity defect law of the mean velocity [33,41], inner and outer scaling of the velocity spectra [22,33], the self-similar scaling of Reynolds shear stress [6,33], and the mixed scaling of the wall-reaching part of large-scale structures [16,22]. This underlying feature of the QLA forms the fundamental basis of the generation of turbulence statistics exhibiting the same qualitative behavior as DNS. Further to this, the QLA is found to provide some useful insights into some of the unresolved issues. The QLA, applied up to $Re_\tau = 2 \times 10^4$, showed that the near-wall peak turbulence intensity would begin to deviate from a logarithmic growth with the Reynolds number for $Re_\tau \geqslant 10^4$. In fact, when examined carefully, such a behavior is also visible in DNS data at lower Reynolds numbers [10] (Fig. 12 in Ref. [33]), favoring the experimental measurement of Ref. [38]. More importantly, the near-wall peak streamwise turbulence intensity of the QLA has been found to follow the scaling of the asymptotic analysis of the Navier-Stokes equations in Ref. [39].

C. Scope of the present study

The aim of this study is to apply a QLA like the one proposed in Ref. [33] to turbulent channel flow up to a relevant extremely high Reynolds number, $Re_\tau = 10^6$, with the hope to gain useful physical insights into the scaling of turbulence intensities. To this end, here we will still consider the stochastic forcing, but with the POD modes in frequency domain (i.e., resolvent modes) [22,48–50], as they have some computational benefits over the approach in Ref. [33] (we shall refer to this approach as resolvent QLA). We note that $Re_\tau = 10^6$ is the typical Reynolds number relevant to the atmospheric surface layer [51], and it would be difficult to obtain any accurate measurement and/or simulation data within the foreseeable future. Given that the QLA in Ref. [33] has been shown to robustly maintain the scaling properties for the energy-containing part of the velocity spectra, its application to such a high Reynolds number would therefore be a useful exercise to address some of the unresolved issues on scaling of turbulent velocity fluctuations.

The contributions of the present study are as follows:

(1) The stochastic QLA proposed in Ref. [33] is reformulated in the frequency domain by utilizing resolvent modes (i.e., formulation of a resolvent-based QLA), while discussing its limitations and accuracy with possibility of further improvement.

(2) The resolvent QLA is compared with the stochastic QLA [33] and DNS [10] to examine its potential to characterize the scaling behavior of turbulence statistics at extremely high Reynolds numbers.

(3) The resolvent QLA is numerically computed up to $Re_\tau = 10^6$. While the turbulence intensities approximately follow the prediction of the original attached eddy model in Refs. [1,2], any discerned inverse power-law spectra directly related to the logarithmic dependence of intensities [3,4] were not found.

(4) The resolvent QLA reveals that the streamwise turbulence intensity in the near-wall and logarithmic regions is proportional to the inverse of the centreline mean velocity instead of $\ln \mathrm{Re}_\tau$, as was predicted by the asymptotic theory of Ref. [39].

(5) The streamwise turbulence intensity exhibits a visible outer peak at sufficiently high Reynolds numbers, and it becomes greater than the inner peak for $\mathrm{Re}_\tau \gtrsim O(10^5)$.

This paper is organized as follows. In Sec. II the quasilinear model in the resolvent framework is introduced and the optimization problem is formulated. In Sec. III the resolvent QLA model is validated with data from DNS [10] and the predictions from the stochastic QLA in Ref. [33]. In Sec. IV scaling of turbulence intensities and spectra from the proposed QLA is extensively assessed up to $\mathrm{Re}_\tau = 10^6$ by comparing it with the outcome of the early attached eddy models [2–4,40]. Finally, the conclusion of this study is presented in Sec. V.

II. PROBLEM FORMULATION

A. Quasilinear approximation

In this study, a pressure-driven turbulent channel flow of an incompressible Newtonian fluid is considered, and the streamwise, wall-normal, and spanwise directions are denoted by x, y, and z, respectively. The channel is assumed to be infinitely long and wide, while the height is $2h$ with the lower wall located at $y = 0$ and the upper wall is located at $y = 2h$. The velocity, $\mathbf{u} = (u, v, w)$ comprises the streamwise, u, wall-normal, v, and spanwise, w, components. For the quasilinear approximation, the flow field is decomposed into two groups, such that all nonlinear terms are kept in the first group while nonlinear self-interactions are dropped in the second group. As in the previous study [33], the Reynolds decomposition is employed here: $\mathbf{u} = \mathbf{U} + \mathbf{u}'$ where $\mathbf{U} = (U(y), 0, 0)$ is the time-averaged mean velocity and $\mathbf{u}'$ is the fluctuating velocity. For the mean flow equation, all the nonlinear terms are kept, and the equation for the streamwise component is given by

$$\nu \frac{dU}{dy} - \overline{u'v'} = \frac{\tau_w}{\rho}\left(1 - \frac{y}{h}\right), \tag{1a}$$

where the overbar denotes time averaging, ν is the kinematic viscosity, τ_w the mean wall shear stress, and ρ the fluid density. The equations for the fluctuating velocity are written as

$$\frac{\partial \mathbf{u}'}{\partial t} + \mathbf{U}\cdot\nabla\mathbf{u}' + \mathbf{u}'\cdot\nabla\mathbf{U} = -\frac{1}{\rho}\nabla p' + \nu\nabla^2\mathbf{u}' + \mathcal{N}, \tag{1b}$$

where p' is the pressure fluctuation, and the nonlinear term is modeled in a minimal manner as in Ref. [33]:

$$\mathcal{N} = \nabla\cdot(\nu_t\nabla\mathbf{u}') + \mathbf{f}', \tag{1c}$$

where $\mathbf{f}'$ is a stochastic forcing and ν_t is the eddy viscosity. We note that the forcing here is introduced to generate a nontrivial solution to (2) due to the linearly stable nature of the typical turbulent mean flows [52,53] and that the eddy viscosity is to mimic the energy removal by the self-interacting nonlinear term at integral length scales in the energy cascade. The eddy viscosity is given by

$$\nu_t(\eta) = \frac{\nu}{2}\left(1 + \frac{\kappa^2\mathrm{Re}_\tau^2}{9}(1-\eta^2)^2(1+2\eta^2)^2\left\{1 - \exp\left[(|\eta|-1)\frac{\mathrm{Re}_\tau}{A}\right]\right\}^2\right)^{1/2} - \frac{\nu}{2} \tag{1d}$$

with $\eta = (y-h)/h$, and the parameters A and κ appear in the van Driest wall law and von Kármán log law. Equation (1d) is an empirical expression originally proposed for pipe flow [41], and the constants A and κ are obtained by matching $U(y)$ from Eq. (1a) to the DNS turbulent mean velocity profile. In this study, $A = 25.4$ and $\kappa = 0.426$ are used for all Reynolds numbers, and they were originally obtained for $\mathrm{Re}_\tau = 2003$ [21]. Using the eddy viscosity, the mean velocity is also obtained with the following closure:

$$-\overline{u'v'} = \nu_t \frac{dU}{dy}. \tag{2}$$

We note that the mean velocity obtained here may not be very accurate at extremely high Reynolds numbers, since $A = 25.4$ and $\kappa = 0.426$ are determined with DNS data at $\mathrm{Re}_\tau \simeq 2000$. However, it still retains the basic scaling behavior robustly (i.e., the law of the wall and the velocity defect law), as was shown in Ref. [33]. The use of the eddy viscosity in Eq. (1c) was originally introduced to study the role of the linear dynamics in the formation of coherent structures [21,22,48,54]. Depending on the problem of interest, it has not been adopted [49], but recent studies have shown that its use considerably improves the linear-operator-based descriptions for turbulence statistics and spectra [26], flow-control modeling [55], state estimations [56–58], and impulse response [29] at high Reynolds numbers.

B. Stochastic forcing in frequency domain and resolvent modes

Now, it should be underlined that the description of the equations of motion is yet to be complete, as the forcing is not described. However, for any form of the forcing, the self-consistent coupling between Eqs. (1a) and (1b) requires that they share exactly the same Reynolds shear stress. A suitable form of the forcing shall therefore be designed hereafter. Furthermore, it is worth mentioning that the closure in Eq. (2) provides information for the Reynolds shear stress component only. Using this information, the QLA predicts the statistical behavior of the other components of the Reynolds stress and the corresponding spectra by seeking such a forcing. In Ref. [33] such a forcing was designed with time-domain POD modes of the response of Eq. (1b) to stochastic forcing. In the present study, we will instead consider frequency-domain POD modes of the stochastic response (i.e., resolvent modes).

We consider a Fourier transform in the streamwise and spanwise directions as well as in the time:

$$\mathbf{u}'(x, y, z; t) = \int_{-\infty}^{\infty}\int_{-\infty}^{\infty}\int_{-\infty}^{\infty} \hat{\mathbf{u}}(y; k_x, k_z, \omega) \mathrm{e}^{i(k_x x + k_z z - \omega t)}\, dk_x\, dk_z\, d\omega, \tag{3}$$

where k_x, k_z, and ω denote the streamwise wave number, the spanwise wave number, and the temporal frequency, respectively. For nonzero wave numbers and frequency, $\hat{\mathbf{u}}(y; k_x, k_z, \omega)$ can be thought of as a propagating wave with the streamwise wavelength $\lambda_x = 2\pi/k_x$, the spanwise wavelength $\lambda_z = 2\pi/k_z$, and the propagating speed $c = \omega/k_x$.

Taking the Fourier transform (3) of Eq. (1b) and defining the state vector as $\hat{\mathbf{q}} = [\hat{v}, \hat{\omega}_y]^T$, where $\hat{v}$ and $\hat{\omega}_y$ are the Fourier-transformed wall-normal components of the velocity and vorticity, respectively, yields the following Orr-Sommerfeld-Squire system:

$$-i\omega\hat{\mathbf{q}} = \mathbf{A}\hat{\mathbf{q}} + \mathbf{B}\hat{\mathbf{f}}, \tag{4a}$$

where the operators $\mathbf{A}$ and $\mathbf{B}$ are defined as

$$\mathbf{A} = \begin{bmatrix} \Delta^{-1}\mathcal{L}_{OS} & 0 \\ -ik_z U' & \mathcal{L}_{SQ} \end{bmatrix},$$

$$\mathbf{B} = \begin{bmatrix} -ik_x\Delta^{-1}\mathcal{D} & -k^2\Delta^{-1} & -ik_z\Delta^{-1}\mathcal{D} \\ ik_z & 0 & -ik_x \end{bmatrix}, \tag{4b}$$

where

$$\mathcal{L}_{OS} = -ik_x(U\Delta - \mathcal{D}^2 U) + \nu_T\Delta^2 + 2\mathcal{D}\nu_T\Delta\mathcal{D} + \mathcal{D}^2\nu_T(\mathcal{D}^2 + k^2),$$
$$\mathcal{L}_{SQ} = -ik_x U + \nu_T\Delta + \mathcal{D}\nu_T\mathcal{D}, \tag{4c}$$

and $\Delta = \mathcal{D}^2 - k^2$, $k^2 = k_x^2 + k_z^2$, $\mathcal{D}$ denotes $\partial/\partial y$. Additionally, in Eq. (4b), the no-slip boundary conditions are enforced on both the upper and lower walls, such that $\hat{v}(\pm h)=\mathcal{D}\hat{v}(\pm h)=\hat{\omega}_y(\pm h)=0$.

The Fourier-transformed velocity fluctuation is recovered from the definition of ω_y:

$$\hat{\mathbf{u}} = \mathbf{C}\hat{\mathbf{q}} = \frac{1}{k^2}\begin{bmatrix} ik_x\mathcal{D} & -ik_z \\ k^2 & 0 \\ ik_z\mathcal{D} & ik_x \end{bmatrix}\hat{\mathbf{q}}. \tag{5}$$

Therefore, using Eqs. (4) and (5), it is possible to obtain a linear input-output relationship between the Fourier-transformed velocity and forcing

$$\hat{\mathbf{u}} = \mathbf{H}(k_x, k_z, \omega)\hat{\mathbf{f}} = -\mathbf{C}(i\omega\mathbf{I} + \mathbf{A})^{-1}\mathbf{B}\hat{\mathbf{f}}, \tag{6}$$

where $\mathbf{H}$ is referred to as a transfer function and $-(i\omega\mathbf{I} + \mathbf{A})^{-1}$ is known as the resolvent operator of $\mathbf{A}$. The forcing and response modes of the resolvent operator are obtained by performing a singular value decomposition (SVD) of $\mathbf{H}$.

Since the forcing and response modes provide two sets of orthonormal basis functions in the wall-normal direction, the fluctuating velocity and the forcing are written as

$$\begin{aligned} \hat{\mathbf{u}} &= \sum_{i=1}^{N} a_i\sigma_i(k_x, k_z, \omega)\hat{\boldsymbol{\psi}}_i(y; k_x, k_z, \omega), \\ \hat{\mathbf{f}} &= \sum_{i=1}^{N} a_i\hat{\boldsymbol{\phi}}_i(y; k_x, k_z, \omega), \end{aligned} \tag{7}$$

where $a_i = \int_0^{2h} \hat{\boldsymbol{\phi}}_i^H \hat{\mathbf{f}}\, dy$, the superscript $(\cdot)^H$ denotes the conjugate transpose, N is the number of the resolvent modes, $\sigma_i \geqslant 0$ are the singular values, and $\hat{\boldsymbol{\phi}}_i = (\hat{\phi}_{u_i}, \hat{\phi}_{v_i}, \hat{\phi}_{w_i})$ and $\hat{\boldsymbol{\psi}}_i = (\hat{\psi}_{u_i}, \hat{\psi}_{v_i}, \hat{\psi}_{w_i})$ the forcing modes and response modes, respectively. From Eq. (7) the spectral covariance matrix in the (k_x, k_z, ω) space is given by

$$E_{\mathbf{uu}}(y; k_x, k_z, \omega) = \langle \hat{\mathbf{u}}\hat{\mathbf{u}}^H \rangle = \sum_{i=1}^{N}\sum_{j=1}^{N} \langle a_i a_j^* \rangle \sigma_i\sigma_j \hat{\boldsymbol{\psi}}_i \hat{\boldsymbol{\psi}}_j^H, \tag{8}$$

where $\langle\cdot\rangle$ denotes ensemble averaging. We also assume that the resolvent modes are delta-correlated [24], such that

$$\langle a_i a_j^* \rangle = \frac{1}{N}\delta_{ij}, \tag{9}$$

where δ_{ij} is the Kronecker delta function. Using this assumption and integrating the relevant real component of the covariance matrix, $\hat{E}_{uv} = \langle \hat{u}\hat{v}^* \rangle$, over the entire (k_x, k_z, ω) space yields the Reynolds shear stress given by

$$\begin{aligned} \langle u'v' \rangle(y) &= \int_{-\infty}^{\infty}\int_{-\infty}^{\infty}\int_{-\infty}^{\infty} \mathrm{Re}\{\hat{E}_{uv}\}\, d\omega\, dk_x\, dk_z, \\ &= \frac{2}{N}\sum_{i=1}^{N}\int_{0}^{\infty}\int_{-\infty}^{\infty}\int_{-\infty}^{\infty} \sigma_i^2 \mathrm{Re}\{\hat{\psi}_{u_i}\hat{\psi}_{v_i}^*\}\, d\omega\, dk_x\, dk_z, \end{aligned} \tag{10}$$

where $\mathrm{Re}\{\cdot\}$ denotes the real part of a complex number.

C. Self-consistent determination of forcing

The primary challenge in the present study lies in reducing the computational cost which would enable us to achieve an extremely high Reynolds number $\mathrm{Re}_\tau = 10^6$ without compromising the scaling behavior of the spectra generated by the QLA. To this end, as in Ref. [33], we will also adhere to the two-dimensional approximation of the forcing in the y-z plane:

$$\hat{\mathbf{f}} = \sum_{i=1}^{N} [\delta(k_x)W(k_z)]^{1/2} a_i \hat{\boldsymbol{\phi}}_i, \tag{11}$$

where $\delta(k_x)$ is the Dirac's delta function and $W(k_z) \geqslant 0$ is a real-valued weight function, through which the spectrum of the forcing will be determined. Here we note that neglecting $k_x \neq 0$ Fourier modes is expected to produce highly anisotropic turbulence intensities [33], since such modes are responsible for the transfer of turbulent kinetic energy from the streamwise to the cross-stream components through pressure strain [59]. In a real flow, this mechanism also involves streak instability and/or transient growth [60–64], which originates from the ignored self-interacting nonlinear terms in Eq. (1b). Therefore, the resolvent modes obtained with (1b) and (1c) (a couple of leading ones, in particular) do not offer the best basis functions for the description of these processes, making the utilization of the $k_x \neq 0$ Fourier modes not very attractive. Despite this important limitation, it has been shown that the resolvent modes for $k_x = 0$ exhibit robust scaling behaviors expected from the velocity spectra obtained with DNSs and experiments [22,33] (see also Figs. 11 and 12 below). These include the following: (1) the inner- and outer-scaling behaviors of the modes at $\lambda_z^+ \simeq 100$ and $\lambda_z/h \simeq O(1)$ [22]; (2) self-similar scaling with y in relation to the logarithmic mean velocity for $100\delta_\nu < \lambda_z < h$ [22,33]; and (3) the inner-scaling behavior of the wall-normal profile of the modes for $\lambda_z \gtrsim O(y)$ in the near-wall region [26]. Therefore, retaining only $k_x = 0$ modes would not affect the basic scaling behaviors of the present QLA at least in a qualitative manner. As such, we shall consider only $k_x = 0$ Fourier modes in this study for the purpose of maintaining a low computational cost.

Altering the forcing with (11) leads to the following spectral covariance matrix:

$$E_{\mathbf{uu}}(y; k_x, k_z, \omega) = \sum_{i=1}^{N} \delta(k_x)W(k_z)\sigma_i^2 \hat{\boldsymbol{\psi}}_i \hat{\boldsymbol{\psi}}_i^H. \tag{12}$$

Using Eq. (9), the Reynolds shear stress, in terms of the weight function $W(k_z)$, is then obtained as

$$\langle u'v'\rangle(y) = \int_{-\infty}^{\infty}\int_{-\infty}^{\infty} W(\beta)e^{\beta}\mathrm{Re}\{\hat{E}_{uv}\}\, d\omega\, d\beta, \tag{13}$$

where $\beta := \log(k_z)$. Here it is worth mentioning that it is possible to enforce a stricter assumption on the type of forcing considered such that only the most amplified modes for each k_z are considered. Since $k_x = 0$ modes are used in this study, the most amplified response modes occur at $\omega = 0$ [22]. Therefore, the forcing in Eq. (11) may further be approximated in the form of

$$\hat{\mathbf{f}} = \sum_{i=1}^{N} [\delta(\omega)\delta(k_x)W(k_z)]^{1/2} a_i \hat{\boldsymbol{\phi}}_i. \tag{14}$$

The term reserved for the forcing in Eq. (14) will be "optimal" forcing, whereas the one in Eq. (11) will be referred to as "broadband" forcing. In the remainder of this section, the formulation of the resolvent-based quasilinear approximation will proceed for the broadband forcing only, since the optimal forcing case can be obtained by simply considering $\omega = 0$ modes and by removing any integration in ω.

In turbulent channel flow, the near-wall peak in the spectra appears at the spanwise length scale of $\lambda_z^+ \approx 100$ [65] [the superscript $(\cdot)^+$ stands for normalization by the viscous inner length scale $\delta_\nu (:=\nu/u_\tau)$ where u_τ is the friction velocity], while the outer one is characterized by $\lambda_z/h \approx 1.5$ [66]. Therefore, to faithfully capture the wide range of length scales, we will consider the spanwise wavelengths to be defined in the interval $\lambda_z \in [10\delta_\nu, 10h]$ with the boundary condition, $W(\lambda_z = 10\delta_\nu) = W(\lambda_z = 10h) = 0$. Furthermore, to robustly determine $W(k_z)$ with the singular values σ_i decaying rapidly with k_z [22], we improve the determination algorithm in Ref. [33] by adding a simple preconditioning procedure. For this purpose, we rewrite Eq. (13) as

$$\langle u'v'\rangle(y) = \int_{-\infty}^{\infty}\int_{-\infty}^{\infty} \widetilde{W}_z(\beta)\mathrm{Re}\{\hat{E}_{uv}\}\frac{\mathrm{e}^{-\beta p}}{R_{uv}(\beta)}\,d\omega\,d\beta, \tag{15a}$$

where

$$R_{uv}(\beta) = \int_{h}^{2h}\int_{-\infty}^{\infty} \mathrm{e}^{\beta}\mathrm{Re}\{\hat{E}_{uv}\}\,d\omega\,dy, \tag{15b}$$

and the original weight function is recovered using

$$W(\beta) = \widetilde{W}(\beta)\frac{\mathrm{e}^{-\beta(p+1)}}{R_{uv}(\beta)}. \tag{16}$$

The introduction of $\widetilde{W}$ is designed to compensate the rapid decay of $\hat{E}_{uv}$ with k_z, and has been proved to be particularly useful for extremely high Re_τ. It has also been found, after varying p in the interval $0.1 \leqslant p \leqslant 0.6$, that setting $p = 0.4$ yields the best results (see Appendix A). Having defined $W(k_z)$ on the given interval and noting that $\widetilde{W}_z(\lambda_z = 10\delta_\nu) = \widetilde{W}(\lambda_z = 10h) = 0$, it is possible to express $\widetilde{W}$, with no loss in generality, as

$$\widetilde{W}[k_z(\beta)] = \sum_{n=1}^{N_\zeta} a_n \sin(n\pi\zeta) \quad \text{with} \quad \zeta = \frac{\beta-\beta_l}{\beta_u-\beta_l}, \tag{17}$$

where N_ζ represents the number of sine polynomials, a_n are the polynomial coefficients to be established, $\beta_l = \log[\pi/(5\delta_\nu)]$ and $\beta_u = \log[\pi/(5\mathrm{h})]$. Using the definition of $\widetilde{W}_z[k_z(\beta)]$ and Eq. (13), the Reynolds shear stress is written as

$$\langle u'v'\rangle(y) = \mathbf{G}\mathbf{a}, \tag{18}$$

where $\mathbf{a} = [a_1\, a_2\, \dots\, a_{N_\zeta}]^{\mathrm{T}}$ and is unknown, while $\mathbf{G}$ is known and equal to

$$\mathbf{G} = \int_{-\infty}^{\infty}\int_{-\infty}^{\infty} \frac{\mathrm{e}^{-\beta p}}{R_{uv}(\beta)} \begin{bmatrix} \sin(\pi\zeta)\mathrm{Re}\{\hat{E}_{uv}\} \\ \sin(2\pi\zeta)\mathrm{Re}\{\hat{E}_{uv}\} \\ \vdots \\ \sin(N_\zeta\pi\zeta)\mathrm{Re}\{\hat{E}_{uv}\} \end{bmatrix}^{\mathrm{T}} d\omega\,d\beta. \tag{19}$$

Now we formulate the optimization problem to determine $\widetilde{W}(k_z)$ by minimizing the difference between the Reynolds shear stress from the mean equation, $\overline{u'v'}$, and the one from the fluctuating velocity equation, $\langle u'v'\rangle$. In addition to minimizing this difference, $\widetilde{W}(k_z)$ must also be sufficiently smooth to be physically relevant. Hence, the following optimization problem is formulated:

$$\min_{\mathbf{a}} \|\overline{u'v'} - \mathbf{G}\mathbf{a}\|_Q^2 + \gamma\mathbf{a}^T\mathbf{S}\mathbf{a}, \tag{20a}$$

subject to

$$\widetilde{W}_z(k_z(\beta)) \geqslant 0, \quad {}^\forall\beta \in [\beta_l, \beta_u], \tag{20b}$$

where $\gamma \geqslant 0$ is the penalty parameter balancing the smoothing objective and minimum error objective, $\mathbf{S} = \mathrm{diag}[e^s\, e^{2s}\, \cdots\, e^{N_\zeta s}]$ with $s = 0.3$ chosen empirically and $\|\cdot\|_Q^2 = \int_{-\infty}^{\log(2h)}(\cdot)^2\,d\log y = \int_0^{2h}(\cdot)^2 Q(y)\,dy$ with $Q(y) = (y/h)^{-1}$ for $0 \leqslant y \leqslant h$ and $Q(y) = (2 - y/h)^{-1}$ for $h \leqslant y \leqslant 2h$. We note that $Q(y)$ is introduced here to ensure that all the wall-normal locations are equally weighted in the logarithmic y coordinate. The smoothing parameter, s, is to ensure that $|a_n|$ decays exponentially with increasing n for $\widetilde{W}(k_z)$ to be sufficiently smooth (for further details, see also Ref. [33]). In particular, Fig. 1 shows that the computed weight function $W(k_z)$ and the preconditioned one $\widetilde{W}(k_z)$

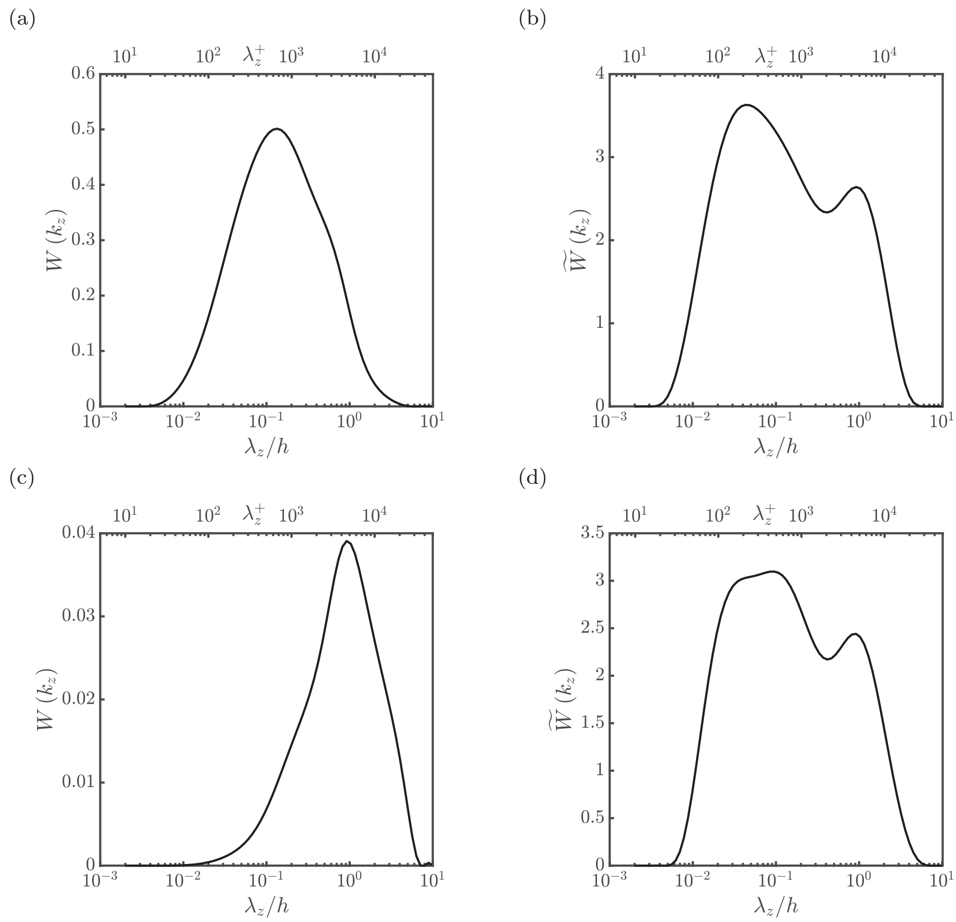

FIG. 1. The weight function $W(k_z)$ and the preconditioned one $\widetilde{W}_z(k_z)$ in Eq. (16): (a), (b) optimal and (c), (d) broadband forcing.

at $\mathrm{Re}_\tau = 5000$ for both optimal and broadband forcing cases (see Sec. III for further details). They are all seen to be sufficiently smooth, suggesting that the choice of $s(=0.3)$ is indeed adequate for both of the cases.

Finally, γ still remains to be arbitrarily. Following Ref. [33], the γ is therefore chosen to ensure that $\|\overline{u'v'} - \mathbf{Ga}\|_Q^2$ is minimized. This optimal penalty parameter, γ_{opt}, can be found by solving the following auxiliary optimization problem:

$$\gamma_{\mathrm{opt}} = \arg\min_{\gamma} \|\overline{u'v'} - \mathbf{Ga}\|_Q^2. \tag{21}$$

We note that the optimization problem defined in Eq. (20) basically remains identical to that in Ref. [33]. The only difference is the utilization of the resolvent framework instead of the time-domain stochastic framework. Therefore, the entire solution procedure of (20) and (21) in this study is identical to that in Ref. [33], except the construction of the spectral covariance matrix in Eq. (8) using the resolvent modes. However, there is also an advantage of the resolvent QLA in the present study over the stochastic QLA in Ref. [33]—the construction of the spectral covariance matrix with the resolvent modes can be performed with a cheaper computational cost using the algorithms constructed in the Krylov subspace (e.g., power method, Arnoldi iteration, etc.). This is particularly true when the optimal forcing in Eq. (14) is considered only with a few leading resolvent modes.

Of course, the resulting prediction of turbulence intensity and spectra with the resolvent modes will not be exactly the same as that with the stochastic response (see Sec. III B). However, it is important to mention that all the scaling behaviors of the resolvent modes have previously been shown to be identical to those of the POD modes from the stochastic responses [22,54]. Therefore, the basic scaling behaviors of the turbulence intensity and spectra from the resolvent QLA will remain qualitatively consistent with those from the stochastic QLA (see Sec. IV B), thereby not deterring the aim of the present study.

D. Limitations, accuracy, computational cost, and outlook

Thus far, we have reformulated the QLA in Ref. [33] by replacing the time-domain POD modes of (1b) and (1c) with the resolvent modes. While the resolvent-based formulation offers a potential for a significant reduction in computational cost, the reason that this was possible is because the formulation of the proposed QLA here and in Ref. [33] is essentially a "under-determined" problem. In other words, as long as the introduced forcing yields the Reynolds shear stress associated with the mean velocity, any choice of the color and amplitude of the forcing is possible subject to this constraint. Some remarks on the limitations, accuracy, computational cost, and outlook are therefore necessary.

(1) *Limitations*: As mentioned, the formulation of the QLA yields a nonunique solution to the system of (1a) and (1b). Therefore, the most fundamental limitation of the QLA is the nonuniqueness originating from how one would precisely determine the color and amplitude of forcing. The best result in terms of generating the smallest optimization error from (21) has often been found when the forcing is determined with most physically meaningful modes, such as the leading POD modes used in Ref. [33] and the leading resolvent modes (see Sec. III B). However, in principle, there is no reason that they have to be the only candidates for the construction of a solution to the proposed QLA.

(2) *Accuracy*: The accuracy of the QLA evidently depends on the nature of the forcing to be determined. In this respect, the only utilization of the $k_x = 0$ Fourier modes is a key restriction which certainly undermines the accuracy. As such, the QLA in its current form is not expected to generate the turbulence statistics "quantitatively" comparable to those of DNS. However, it is important to note that the leading POD modes or resolvent modes have been shown to exhibit robust scaling behaviors consistent with the spectra of DNS (for a detailed discussion, the reader may refer to Refs. [16,22,33]). Therefore, their utilization for the construction of turbulence statistics through the proposed QLA should provide sound information retaining physically consistent scaling behaviors. This is the fundamental reason why the QLA would be useful especially to study the scaling with Reynolds number.

(3) *Computational cost:* The key reason that the present study aims to explore the utilization of resolvent modes is its considerably cheap computational cost compared to that required for solving the Lyapunov equation in Ref. [33]. However, as will be discussed in Sec. III, the resolvent QLA does not appear to be more accurate than the stochastic QLA (e.g., Fig. 5 below), although it still maintains the basic scaling behaviors consistent with those of DNS data. Therefore, the QLA formulated with the time-domain POD modes in Ref. [33] remains a more attractive option for the future work. In this case, a computationally viable option, which also maintains the accuracy of the QLA in Ref. [33], would be to obtain the solution to the Lyapunov equation in frequency domain, as was proposed in Ref. [67].

(4) *Outlook*: The nonuniqueness of the solution to the quasilinear system given by (1a) and (1b) is certainly an important limitation, but the related extra degree of freedom is also an opportunity to improve the accuracy of the QLA, especially combining with the previous data-driven approaches based on the linearized Navier-Stokes framework [24,44]. The key strength of the present QLA lies in the recovery of the basic scaling behavior and extrapolation capability with the minimal data (i.e., mean velocity). While taking these features as a basic template, the extra degree of freedom associated with the nonuniqueness can be further exploited to improve the accuracy of the present

QLA by feeding more data to the formulation. This is an issue of ongoing investigation, and its preliminary result is available in Ref. [68].

III. RESOLVENT-BASED MINIMAL QUASILINEAR APPROXIMATION

A. Numerical methods

The wall-normal coordinate in the Orr-Sommerfeld-Squire system in Eq. (4c) was discretized using a Chebyshev collocation method [69] with N_y grid points. For the QLA with broadband forcing, the integration in ω is performed from $\omega = 0$ to $\omega = 25/\lambda_z$ at $\mathrm{Re}_\tau = 5000$ (note that the broadband QLA is considered only for $\mathrm{Re}_\tau = 5000$), and the grid points in the ω coordinate are spaced uniformly with $N_\omega = 100$. The grid points of the spanwise wave number is made to be spaced logarithmically in the k_z coordinate, and the related integrals were evaluated using the trapezoidal rule. The resolution for this integration is thus lower than $\Delta\beta = 0.05$, so that the errors in the numerical integration do not exceed $O(\Delta\beta^2)$. The number of grid points in the wall-normal, spanwise wave number, and forcing frequency coordinates are summarized in Table I. The quadratic programming problem given in Eq. (20) [70] is solved using the MATLAB function `quadprog`. The number of sine polynomials, N_ζ, used to obtain the weight function has been found to achieve good convergence for $N_\zeta \geqslant 50$, and $N_\zeta = 100$ is used in this study (see also Ref. [33] for further details). Last, the auxiliary optimization problem which defines the optimal penalty parameter, γ_{opt}, is solved using a simple line search over the logarithmic γ axis.

The proposed resolvent QLA is applied to model turbulent channel flow in a wide range of Reynolds numbers from $\mathrm{Re}_\tau = 10^3$ to $\mathrm{Re}_\tau = 10^6$ with fixed values of $s = 0.3$ and $p = 0.4$. Table I summarizes the resolvent QLAs performed in the present study. The level of the errors in the logarithmic y coordinate (Q norm) remains below $O(10^{-3})$, and that in the algebraic y coordinate ($\mathcal{L}_2$ norm) varies from $O(10^{-3})$ to $O(10^{-6})$. In particular, the errors are seen to be smallest with $N = 2$, as they remain at $O(10^{-5} - 10^{-6})$. This issue will be discussed further in the following subsections.

TABLE I. Computational parameters and optimization errors. N_y is the number of wall-normal Chebyshev collocation points, N_{k_z} the number of spanwise wave numbers logarithmically spaced in the k_z axis, N_ω the number of forcing frequencies spaced linearly in the ω axis, $\|\cdot\|_Q^2$ is the Q norm defined in Sec. II B, $\|\cdot\|_{\mathcal{L}_2}^2$ is the standard $\mathcal{L}_2$ norm, and N is the number of modes used in the computation of the spectral covariance matrix.

Re_τ	N_y	N_{k_z}	N_ω	γ_{opt}	$\|\overline{u'v'} - \langle u'v' \rangle\|_Q^2$	$\|\overline{u'v'} - \langle u'v' \rangle\|_{\mathcal{L}_2}^2$	N
1×10^3	257	66	1	2.1×10^{-3}	9.5×10^{-4}	8.2×10^{-5}	2
2×10^3	257	71	1	1.4×10^{-3}	9.3×10^{-4}	4.6×10^{-5}	2
5×10^3	513	76	100	1.8×10^{-4}	5.5×10^{-4}	7.1×10^{-6}	2
5×10^3	513	76	100	7.4×10^{-3}	6.4×10^{-3}	1.8×10^{-3}	8
5×10^3	513	76	100	5.4×10^{-3}	4.4×10^{-3}	1.1×10^{-3}	16
5×10^3	513	76	1	6.8×10^{-4}	9.1×10^{-4}	2.3×10^{-5}	2
5×10^3	513	76	1	4.8×10^{-3}	4.5×10^{-3}	1.1×10^{-3}	8
5×10^3	513	76	1	4.6×10^{-3}	4.6×10^{-3}	1.0×10^{-3}	16 (all)
1×10^4	769	87	1	4.2×10^{-4}	9.1×10^{-4}	1.2×10^{-5}	2
2×10^4	1025	91	1	2.4×10^{-4}	9.2×10^{-4}	6.8×10^{-6}	2
1×10^5	1601	110	1	5.9×10^{-5}	9.3×10^{-4}	4.7×10^{-6}	2
2×10^5	2001	120	1	3.5×10^{-5}	9.5×10^{-4}	2.4×10^{-6}	2
5×10^5	2451	135	1	1.7×10^{-5}	9.7×10^{-4}	5.3×10^{-6}	2
1×10^6	4001	150	1	1.7×10^{-5}	1.2×10^{-3}	6.9×10^{-6}	2

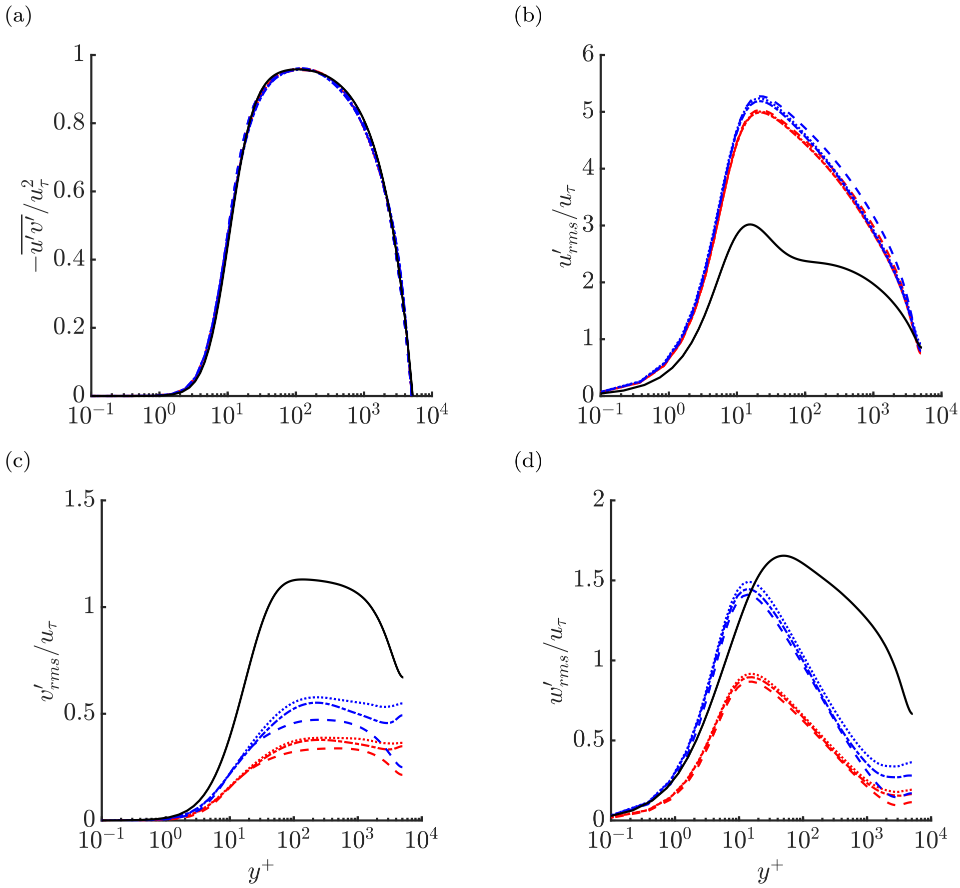

FIG. 2. Second-order turbulence statistics for optimal/broadband QLAs at $\mathrm{Re}_\tau = 5000$ and for DNS [10] at $\mathrm{Re}_\tau = 5186$: (a) $-\overline{u'v'}/u_\tau^2$; (b) u'_{rms}/u_τ; (c) v'_{rms}/u_τ; (d) w'_{rms}/u_τ. Here DNS (—), optimal forcing QLA with $N = 2$ (— — —), $N = 8$ (— · —), and $N = 16$ (· · ·), and broadband forcing QLA with $N = 2$ (— — —), $N = 8$ (— · —), and $N = 16$ (· · ·).

B. Quasilinear approximation at $\mathrm{Re}_\tau = 5000$

We first consider the broadband and optimal forcing cases for $\mathrm{Re}_\tau = 5 \times 10^3$, and they are assessed with DNS data at $\mathrm{Re}_\tau = 5186$ [10]. The effect of increasing the number of response modes, N, used in the computation of the spectral covariance matrix is examined in Fig. 2, where the Reynolds stresses of the resolvent QLA are compared to those of DNS [10]. Here we note that for small N, the number of response modes must be an even integer, given the midplane symmetry of channel flow. The Reynolds shear stresses for both of the QLAs show good agreement with that of DNS Reynolds shear stress, regardless of the number of POD and resolvent modes used, indicating that the Cess model for the mean velocity, tuned at $\mathrm{Re}_\tau = 2003$ [21], is reasonable for $\mathrm{Re}_\tau = 5000$. However, considerable differences arise when the velocity fluctuations of the QLAs are compared to those of DNS. Both QLAs exhibit the following features: their streamwise velocity fluctuation is larger than that of DNS [Fig. 2(b)], whereas the wall-normal and spanwise velocity ones are smaller than those of DNS [Figs. 2(c) and 2(d)]. In particular, the optimal forcing QLA displays a stronger anisotropy compared to the broadband forcing case, and this is because the optimal forcing QLA incorporates only the frequency of the largest amplification made via the lift-up effect. However, the aforementioned anistotopy in turbulence intensities is also common to both the resolvent and the stochastic QLAs. This is a direct consequence of ignoring all nonzero streamwise varying Fourier modes [33], as was discussed with Eq. (11).

As N is increased in Fig. 2, the turbulent intensities become more isotropic. However, increasing the response modes does not seem to improve the QLA, since some odd features, such as peaks in the wall-normal and spanwise fluctuations, appear for $y^+ \geqslant 2000$. Here we note that the emergence of such odd features with increasing N is partly due to the delta-correlated nature of the resolvent modes considered in Eq. (9). The assumption may be relaxed by allowing the amplitude of higher-order resolvent modes to vary as in Refs. [43,46]—the resolvent modes are orthogonal, thus the interpolation capability may well be utilized for the purpose of low-dimensional approximation for the velocity spectra. However, in such a case, the extrapolation/prediction capability of the present QLA, which relies only on the mean velocity given by Eqs. (1d) and (2), becomes immediately unavailable, because more flow data (e.g., velocity spectra) are required to find the amplitude variations. Therefore, we shall not consider such an approach here.

To further understand the effect of increasing N, the spanwise wave number spectra of the wall-normal velocity of the broadband resolvent QLA are compared to those of DNS [10] in Fig. 3. The DNS spectra [Fig. 3(a)] are consistent with the attached eddy hypothesis, since the

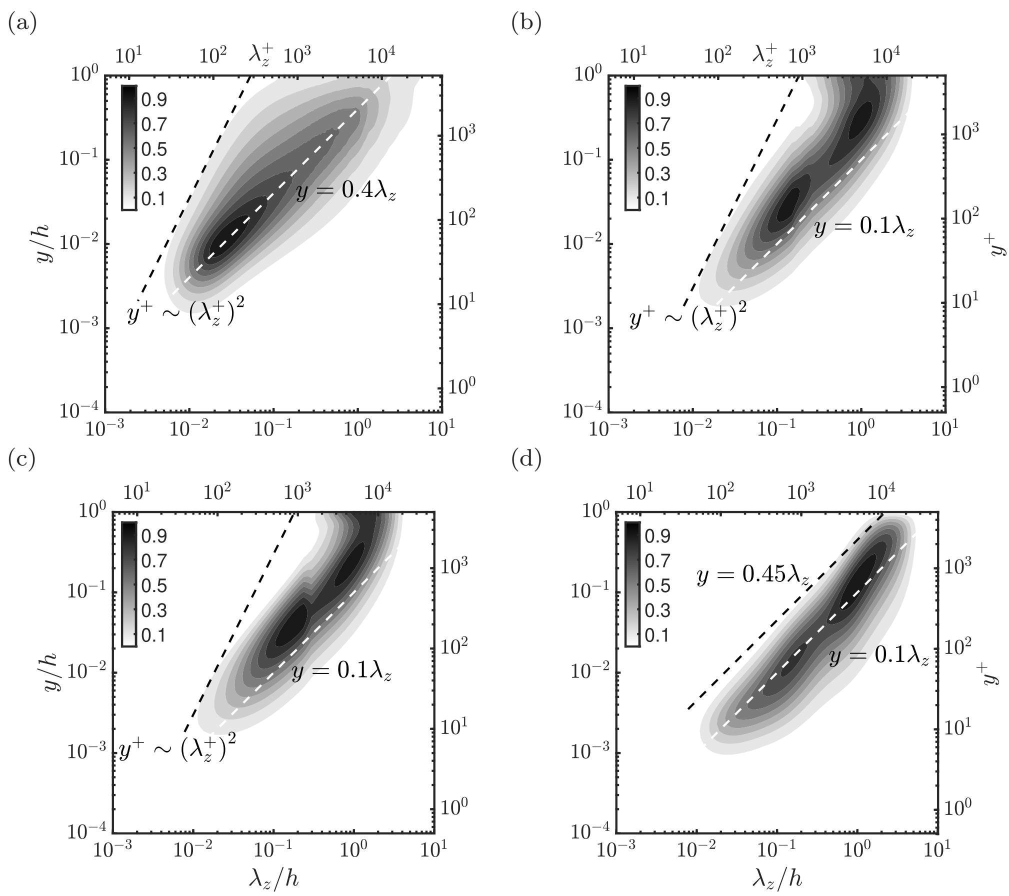

FIG. 3. Premultiplied spanwise wave number spectra of wall-normal velocity from (a) DNS [10] at $\mathrm{Re}_\tau = 5186$ and from (b)–(d) the resolvent QLA at $\mathrm{Re}_\tau = 5 \times 10^3$. In (b) $N = 16$; (c) $N = 8$; (d) $N = 2$. The contours are normalized by their maximum value.

energy-containing region of the spectra appears to be aligned along a linear ridge ($y = 0.4\lambda_z$). In general, the qualitative behavior between DNS and the broadband QLA is consistent, as was the case for the stochastic QLA [33]. A notable difference is the presence of the large-scale peak $\lambda_z/h \simeq 1$ in the QLAs unlike DNS. However, the spectra around the peak remain changed very little with the Reynolds number, especially for $\mathrm{Re}_\tau > 10^4$ [Fig. 7(i) below], thereby not significantly affecting the overall scaling behavior in the turbulence intensity and spectra at such high Reynolds numbers. Nevertheless, for $N \geqslant 8$, some nonphysical artifacts start to arise due to the crude approximation of the nonlinear term $\mathcal{N}$ modeled in Eq. (1c) and in Eq. (9). Indeed, in such cases, the low-level contours are not well aligned with $y \sim \lambda_z^2$ (i.e. the Taylor microscale in the log layer) unlike those of DNS [Fig. 3(a)] (see Ref. [6] for a further discussion). A strong velocity fluctuation also emerges near the channel center. However, this must be nonphysical, given that production is zero at the midplane in real turbulent channel flow. Such nonphysical artifacts are removed when $N = 2$ is chosen. This is presumably because the leading two resolvent modes are the most physical ones in the sense that they are most amplified and/or influenced by the linearized Navier-Stokes operator. Indeed, the leading two modes contain more than 80% of the energy of all resolvent modes for $50\delta_\nu \leqslant \lambda_z \leqslant 10h$ (see Appendix B).

Following the observations here, $N = 2$ is employed for the remainder of this study. We note that this case also yields the smallest optimization errors (Table I). Moreover, the optimal QLA is capable of producing the optimization errors of the same order of magnitude (Table I) and qualitatively analogous turbulence intensities (Fig. 2) to the broadband QLA. Therefore, the optimal forcing model will be used hereafter, given its lower computational cost and hence its accessibility to the regime of very high Re_τ.

C. Comparison of frequency- and time-domain quasilinear approximations

Before applying the resolvent QLA with optimal forcing to other Reynolds numbers, its turbulence statistics and spectra are finally compared with those of the stochastic QLA [33] at $\mathrm{Re}_\tau = 5000$. Figure 4 shows the spanwise wave number spectra of the streamwise, wall-normal, and spanwise velocities from the resolvent and the stochastic QLAs together with those also from DNS [10]. Qualitatively, both of the QLAs seem to produce analogous spectra, qualitatively comparable to those from DNS. However, for the streamwise and spanwise velocity components [Figs. 4(a), 4(b), 4(g), and 4(h)], the spectral intensities of the stochastic QLA are smaller than those of the resolvent QLA. On the other hand, for the wall-normal velocity component, the stochastic QLA yields larger spectral intensities than the resolvent one does. This suggests that the resolvent QLA produces more anisotropic turbulence intensities than the stochastic counterpart, as is confirmed in Fig. 5.

To understand the difference observed from the resolvent and stochastic QLAs, we consider the following linear matrix equation, which has often been used as a model of the Orr-Sommerfeld-Squire operator [71]:

$$\frac{\partial}{\partial t}\begin{bmatrix} \hat{v}_m \\ \hat{\omega}_{y,m} \end{bmatrix} = \begin{bmatrix} -\frac{1}{\mathrm{Re}} & 0 \\ 1 & -\frac{2}{\mathrm{Re}} \end{bmatrix}\begin{bmatrix} \hat{v}_m \\ \hat{\omega}_{y,m} \end{bmatrix}, \tag{22}$$

where the state vector $[\,\hat{v}_m \;\; \hat{\omega}_{y,m}\,]$ mimics $[\,\hat{v} \;\; \hat{\omega}_y\,]$ and Re models the effective Reynolds number of the system. The resolvent response modes and the POD modes of the stochastic response are obtained by performing a SVD of the linear operator in Eq. (22) and by solving the Lyapunov equation for the operator, respectively. In the case of (22), the singular values and the corresponding

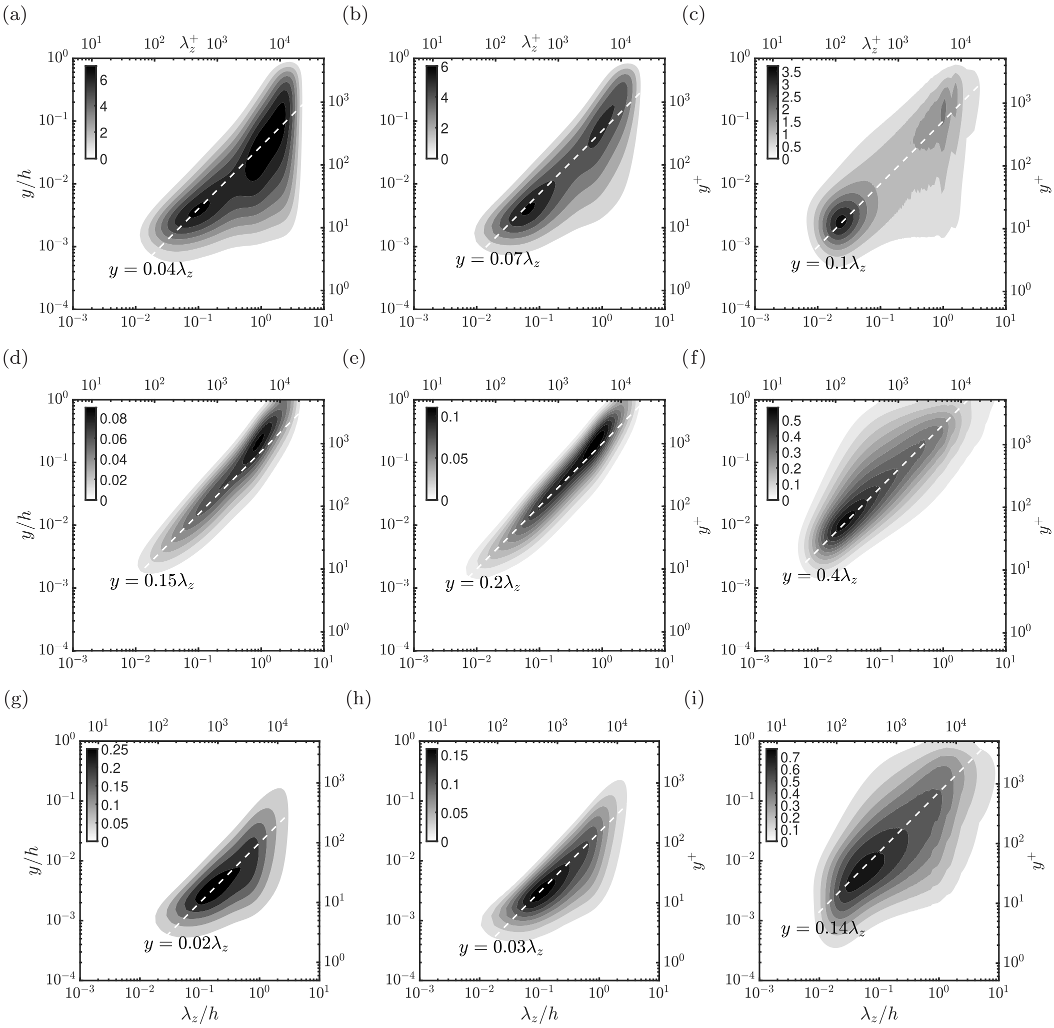

FIG. 4. Premultiplied spanwise wave number spectra at $\mathrm{Re}_\tau = 5 \times 10^3$ from (a), (d), (g) resolvent QLA with optimal forcing and two leading resolvent modes ($N = 2$), from (b), (e), (h) stochastic QLA with two leading POD modes [33] and from (c), (f), (i) DNS [10] (at $\mathrm{Re}_\tau = 5186$): (a)–(c) streamwise velocity, (d)–(f) wall-normal velocity, (g)–(i) spanwise velocity.

response resolvent modes are

$$\left(\sigma_{1,2}^{\mathrm{res}}\right)^2 = \frac{1}{8}\mathrm{Re}^2(\mathrm{Re}^2 + 5 \pm \sqrt{\mathrm{Re}^4 + 10\mathrm{Re}^2 + 9}), \tag{23a}$$

$$\hat{\boldsymbol{\psi}}_{1,2}^{\mathrm{res}} = \frac{1}{\chi_{1,2}^{\mathrm{res}}}\begin{bmatrix} -\frac{3}{4}(1+\mathrm{Re}^2) \mp \frac{1}{4}\sqrt{\mathrm{Re}^4 + 10\mathrm{Re}^2 + 9} \\ \mathrm{Re}^3 + \mathrm{Re} \end{bmatrix}, \tag{23b}$$

$$\chi_{1,2}^{\mathrm{res}} = \sqrt{\left[-\frac{3}{4}(1+\mathrm{Re}^2) \mp \frac{1}{4}\sqrt{\mathrm{Re}^4 + 10\mathrm{Re}^2 + 9}\right]^2 + (\mathrm{Re}^3 + \mathrm{Re})^2}, \tag{23c}$$

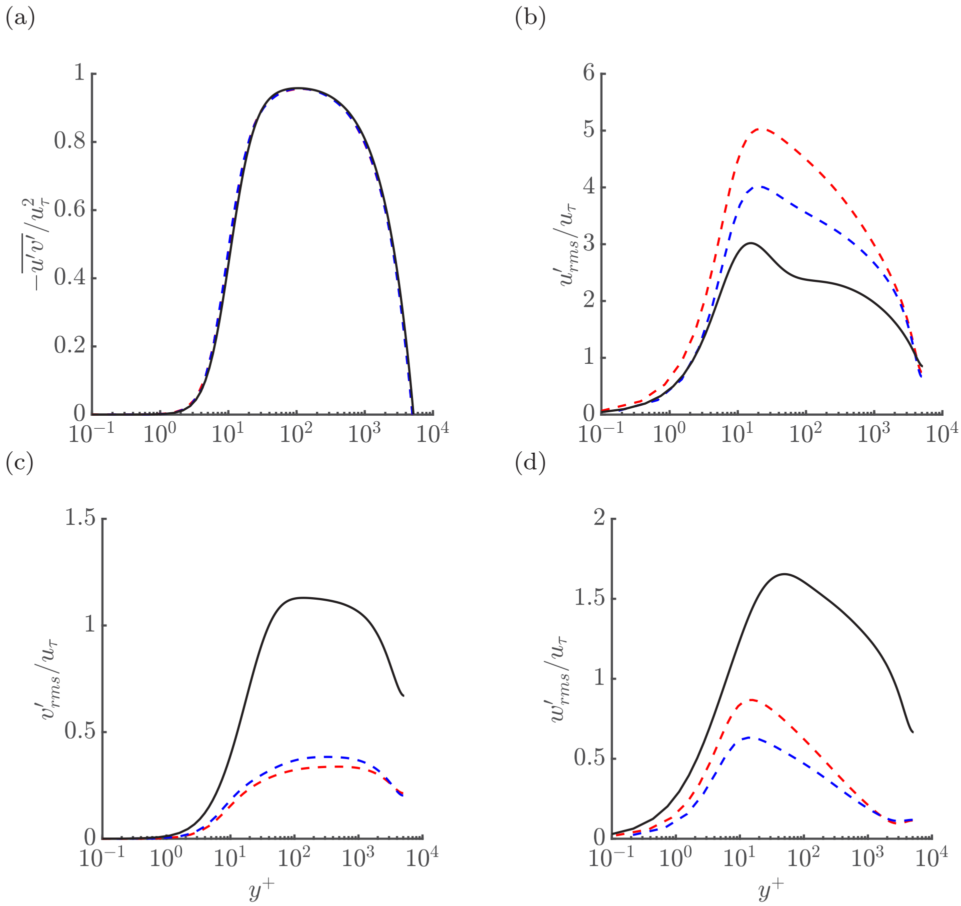

FIG. 5. Second-order turbulence statistics for optimal QLA, time-domain QLA [33] both at $\mathrm{Re}_\tau = 5 \times 10^3$ and DNS [10] at $\mathrm{Re}_\tau = 5186$: (a) $-\overline{u'v'}/u_\tau^2$, (b) u'_{rms}/u_τ, (c) v'_{rms}/u_τ, (d) w'_{rms}/u_τ. Here DNS (—), optimal $N = 2$ (− − −), stochastic $N_{\mathrm{POD}} = 2$ (− − −).

whereas the energy of the POD modes and the corresponding mode structures are given by

$$\sigma_{1,2}^{\mathrm{POD}} = 0.0417\mathrm{Re}(\mathrm{Re}^2 + 9 \pm \sqrt{\mathrm{Re}^4 + 10\mathrm{Re}^2 + 9}), \tag{24a}$$

$$\hat{\boldsymbol{\psi}}_{1,2}^{\mathrm{POD}} = \frac{1}{\chi_{1,2}^{\mathrm{POD}}}\left[\begin{matrix}\frac{1}{4}(3 - \mathrm{Re}^2) \pm \frac{1}{4}\sqrt{\mathrm{Re}^4 + 10\mathrm{Re}^2 + 9} \\ \mathrm{Re}\end{matrix}\right], \tag{24b}$$

$$\chi_{1,2}^{\mathrm{POD}} = \sqrt{\left(\frac{1}{4}(3 - \mathrm{Re}^2) \pm \frac{1}{4}\sqrt{\mathrm{Re}^4 + 10\mathrm{Re}^2 + 9}\right)^2 + \mathrm{Re}^2}. \tag{24c}$$

Here we note that the square of the singular values $[(\sigma^{\mathrm{res}})^2]$ are juxtaposed to the energy of the POD modes (σ^{POD}), because these are the quantities imposed for the computation of the spectral covariance matrix (see Sec. II B). From Eqs. (23) and (24), it is evident that $(\sigma^{\mathrm{res}})^2 \geqslant \sigma^{\mathrm{POD}}$ by a factor of $O(\mathrm{Re})$, consistent with the behavior of the Orr-Sommerfeld operator shown in Refs. [71–74]. Furthermore, the wall-normal vorticity component, directly proportional to the streamwise velocity (since $k_x = 0$ is considered), is larger in the resolvent response mode by a factor of $O(\mathrm{Re})$ given the normalization. Although the effective viscosity of the linearized operator (1b) with (1c) would not be very large due to the eddy viscosity, this explains the more anisotropic nature of the resolvent QLA towards the streamwise component than the stochastic one [Fig. 5(b)].

IV. SCALING OF TURBULENCE INTENSITY UP TO $\mathrm{Re}_\tau = 10^6$

A. Spectra

Having verified and compared the proposed QLA to DNS [10] as well as to the stochastic QLA [33] at $\mathrm{Re}_\tau = 5 \times 10^3$, we now proceed to study the regime of very high Reynolds numbers ranging from $\mathrm{Re}_\tau = 10^3$ to $\mathrm{Re}_\tau = 10^6$. The inner- and outer-scaled spanwise wave number spectra of the velocity and Reynolds shear stress from the QLA are compared to those from DNS [10] in Figs. 6 and 7, respectively. As expected, the qualitative behaviors of the spectra from the resolvent QLA are seen to be identical to those from DNS. The spectra from the QLA span from $\lambda_z^+ \approx O(10)$ to $\lambda_z \approx O(h)$ like those from the DNS (Figs. 6 and 7). Moreover, the near-wall region of the QLA spectra [$y^+ \lesssim O(10^2)$] for $\lambda_z^+ \lesssim O(100)$ scales very well in the inner units, as observed in the DNS data (Fig. 6). Very good outer scaling is also seen in the outer region from the spectra of the QLA and DNS (Fig. 7), while the spectra of streamwise and spanwise velocities develop a wall-reaching part at large λ_z [see the low-level contours in Figs. 7(a)–7(c), 7(j)–7(l)]. This part is "inactive" in the sense of Townsend [2], because the Reynolds shear stress spectra do not exhibit such a wall-reaching part. Despite the basic scaling behavior of the QLA qualitatively consistent with that of DNS, the QLA tends to show separation between inner and outer peaks at higher Reynolds numbers: for example, in the case of DNS, the inner and outer peaks in the streamwise velocity spectra are distinguishable at $\mathrm{Re}_\tau \gtrsim 2 \times 10^3$, but the same happens in the QLA at $\mathrm{Re}_\tau \gtrsim 5 \times 10^3$ [Figs. 6(a)–6(c)].

It is evident that all the spectra from the resolvent QLA shown in Figs. 6 and 7 are aligned with a linear scaling (see also Figs. 3 and 4), while those of streamwise and spanwise velocities exhibit the wall-reaching inactive part. This observation is consistent with the early attached eddy models of Townsend and Perry [2–4]. However, even at $\mathrm{Re}_\tau = 10^6$, a discerned form of the inverse-law power spectrum (i.e., k_z^{-1} spectrum) proposed in Refs. [3,4] does not seem to appear [see also Figs. 8(a) and 8(b)], reminiscent of the "incomplete similarity" argument made with the early data from the Superpipe Facility in Princeton [75,76]. Here we note that the QLA in the present study and the early attached eddy models [1,2] share fundamentally the same mathematical structure especially in the logarithmic layer, since both of the models are based on linear superposition of self-similar statistically stationary structures subject to approximately constant Reynolds shear stress: indeed, it was both analytically and numerically shown that the logarithmic mean velocity profile is associated with the self-similar linear modes of (1b) with (1c) (i.e., the flow field with the largest transient energy growth, resolvent modes, and time-domain POD modes in the stochastic response) for $O(100\delta_\nu) < \lambda_z < O(h)$ [16,22]. In fact, the present QLA and the one in Ref. [33] basically deal with the issue of how one would self-consistently superpose those modes subject to the given mean velocity profile like in the original attached eddy model [1,2] (see Ref. [33] for a further discussion). Therefore, the lack of a discerned form of k_z^{-1} spectrum in the present QLA is likely to originate from the difference of the present QLA from the attached eddy models, which is the boundary behavior of the self-similar structures superposed: the present QLA employs the no-slip boundary condition, whereas the early attached eddy models are based on a velocity slip boundary condition. In the spectrum-based attached eddy model [4], the velocity slip boundary condition yields the outer-scaling part of the spectra to be independent of y for $y \ll h$:

$$\frac{k_z \Phi_{uu}(k_z, y/h)}{u_\tau^2} = f_1(k_z h), \tag{25a}$$

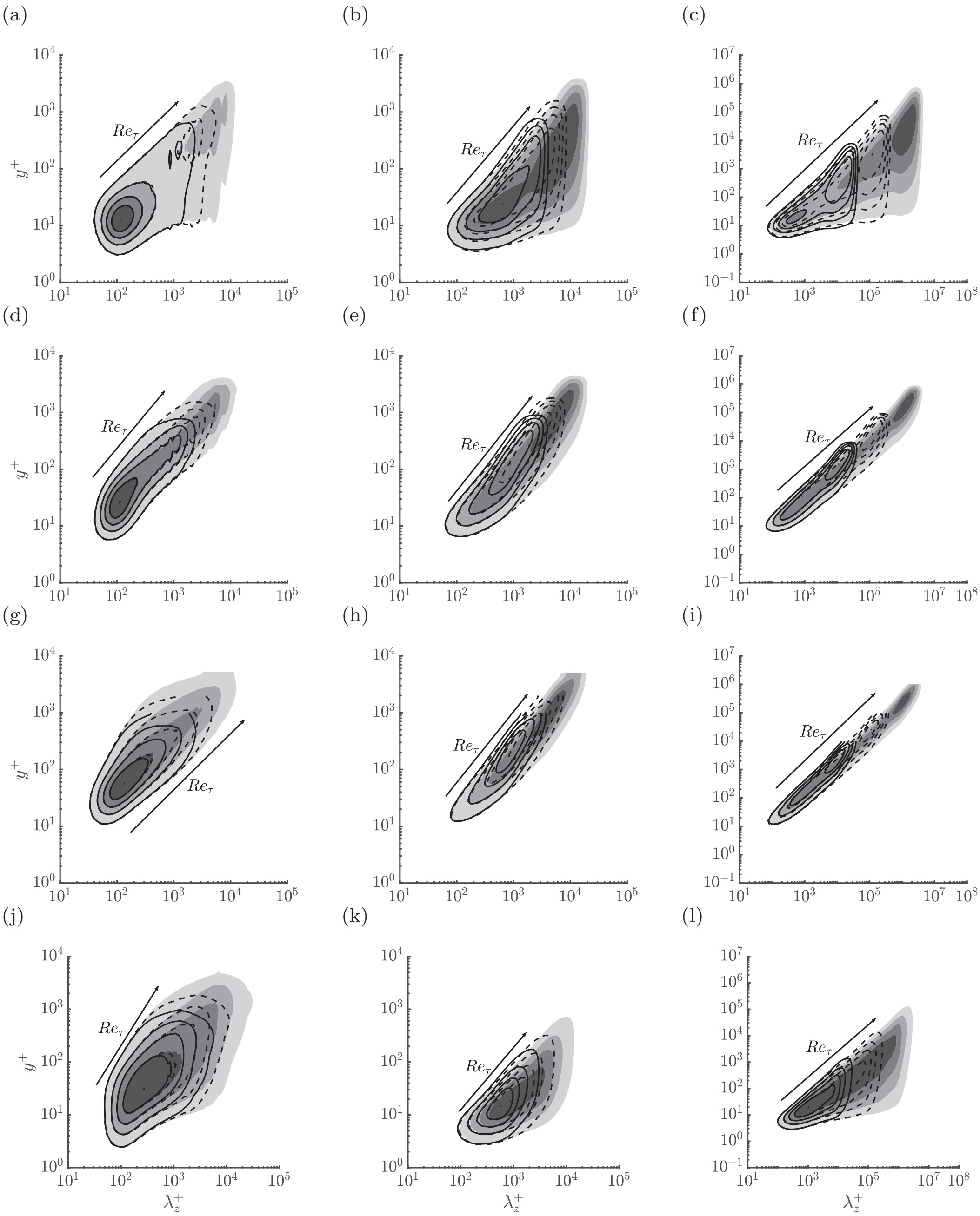

FIG. 6. Premultiplied spanwise wave number spectra from (a), (d), (g), (j) DNS [10] and (b), (c), (e), (f), (h), (i), (k), (l) resolvent QLA in the inner-scaled coordinates: (a)–(c) streamwise velocity, (d)–(f) Reynolds shear stress, (g)–(i) wall-normal velocity, (j)–(l) spanwise velocity. Here $\mathrm{Re}_\tau = 1001, 1995, 5186$ for DNS, $\mathrm{Re}_\tau = 10^3, 2 \times 10^3, 5 \times 10^3$ for (b), (e), (h), (k) and $\mathrm{Re}_\tau = 10^4, 10^5, 10^6$ for (c), (f), (i), (l). Here the spectra are normalized by their maximum value, and the contour level is spaced with 20% of the maximum.

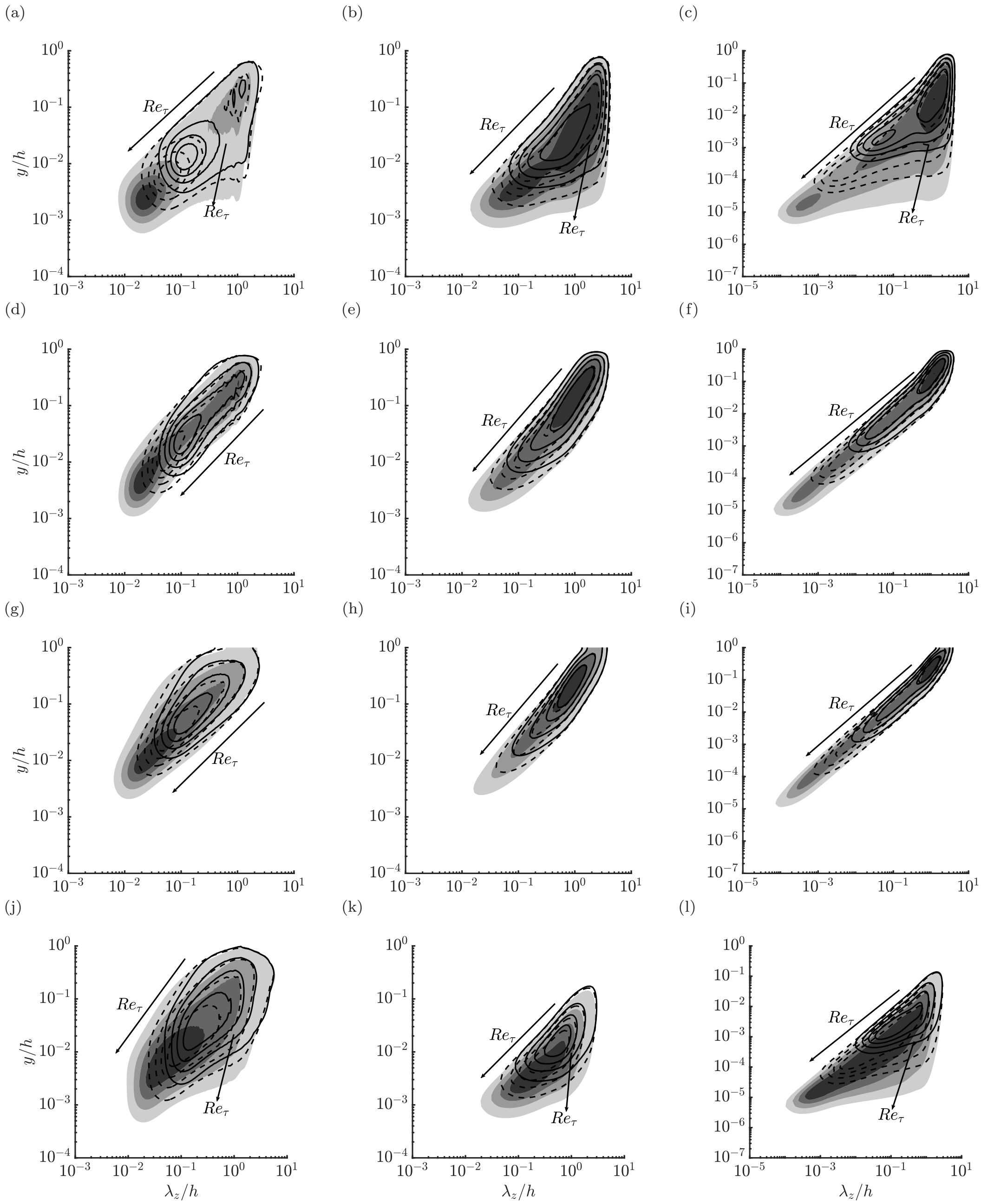

FIG. 7. Premultiplied spanwise wave number spectra from (a), (d), (g), (j) DNS [10] and (b), (c), (e), (f), (h), (i), (k), (l) resolvent QLA in the outer-scaled coordinates: (a)–(c) streamwise velocity, (d)–(f) Reynolds shear stress, (g)–(i) wall-normal velocity, (j)–(l) spanwise velocity. Here $\mathrm{Re}_\tau = 1001, 1995, 5186$ for DNS $\mathrm{Re}_\tau = 10^3, 2 \times 10^3, 5 \times 10^3$ for (b), (e), (h), (k), and $\mathrm{Re}_\tau = 10^4, 10^5, 10^6$ for (c), (f), (i), (l). Here the spectra are normalized by their maximum value, and the contour level is spaced with 20% of the maximum.

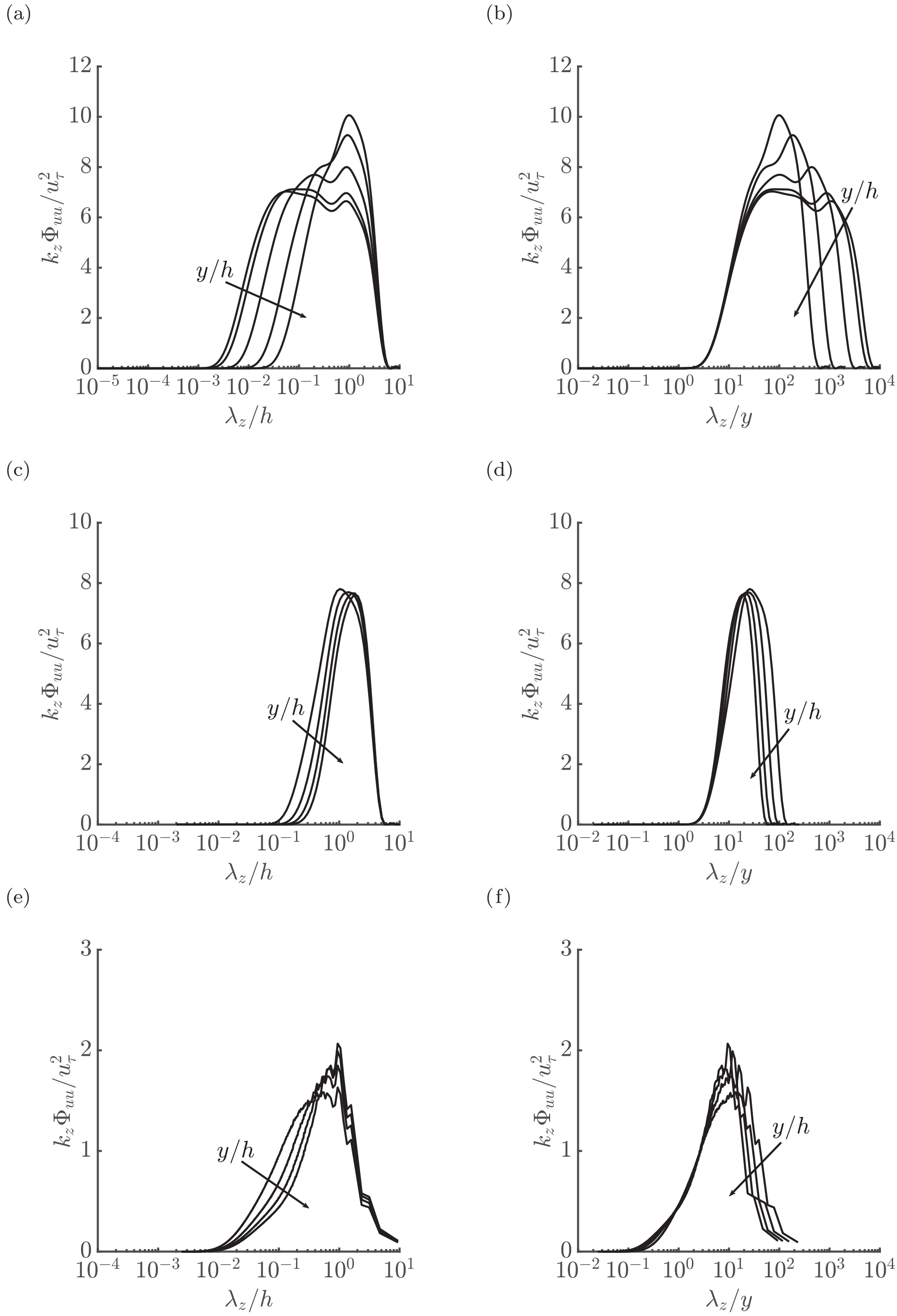

FIG. 8. Premulitplied spanwise wave number spectra of streamwise velocity in the (a), (c), (e) h- and (b), (d), (f) y-scaled wave number coordinates: (a), (b) the resolvent QLA at $\mathrm{Re}_\tau = 10^6$ and (c), (d) at $\mathrm{Re}_\tau = 5 \times 10^3$; (e), (f) DNS at $\mathrm{Re}_\tau = 5186$ [10]. In panels (a) and (b) $y/h = 0.0008, 0.001, 0.002, 0.005, 0.01$ ($y^+ \simeq 800, 1000, 2000, 5000, 10\,000$), whereas in panels (c)–(f) $y/h = 0.04, 0.06, 0.08, 0.1$ ($y^+ \simeq 200, 300, 400, 500$).

where $\Phi_{uu}(k_z, z/h)$ is the spectra of streamwise velocity. The inverse-law power-spectral behavior is then obtained by matching Eq. (37) with the y-scaling spectra given by

$$\frac{k_z \Phi_{uu}(k_z, y/h)}{u_\tau^2} = f_2(k_z y). \tag{25b}$$

Let us now compare the streamwise velocity spectra of the QLA [Fig. 7(c)] at $\mathrm{Re}_\tau = 10^6$ with those depicted by Eqs. (25a) and (25b). Figure 8 plots the spectra in the logarithmic layer in the h- and y-scaled coordinates. The spectra do not seem to exactly follow the scaling in Eq. (25a) at least for $\lambda_z/h > O(1)$ [Fig. 8(a)], whereas the y scaling in Eq. (25b) appears to hold for $\lambda_z/y \leqslant O(10)$ [Fig. 8(b)]—indeed, the contours in Fig. 7(b) suggest that the intensity of the spectra at $\lambda_z/h \sim O(1)$ monotonically decays as $y \to 0$ for $y/h < 0.01$, which differs from the scaling law in Eq. (25a). While there seems to be k_z^{-1} spectrum for a certain y ($y/h = 0.001$ in Fig. 8), it emerges only around that particular location. Therefore, the k_z^{-1} spectrum at $y/h = 0.001$ is not necessarily a direct consequence of an asymptotic matching between Eqs. (25a) and (25b), given that the scaling of Eq. (25b) does not hold precisely. Importantly, the observation made here also applies to the spectra from the proposed QLA and DNS at $\mathrm{Re}_\tau \simeq 5000$ [Figs. 8(c)–8(f)], although the length-scale separation in the QLA spectra is less than that in the DNS spectra. This rather indicates that the observation may not necessarily be a simple artifact of the present QLA. It is presumable that the reason that Eq. (25a) does not appear in the spectra of the present QLA is due to the no-slip boundary condition—the presence of the wall should weaken the amplitude of the resolvent modes to satisfy the boundary condition at $y = 0$. The issue of how such linear modes obtained from (1b) with (1c) behave as $y \to 0$ was discussed in detail in Refs. [16,22] in comparison to the spectra from DNS. In particular, these studies showed that the scaling behavior of the linear modes used in the present QLA is very similar to that of the spectra from DNS in the region close to the wall [see Figs. 2 and 3 in Ref. [26]]. Therefore, the observation made here with the present QLA and the previous studies [16,22] implies that the viscous effect caused by the no-slip boundary condition would be needed for the precise description of the velocity spectra even at $\mathrm{Re}_\tau = 10^6$.

B. Turbulence intensity

Turbulence intensities and Reynolds shear stress, obtained from the spectra in Figs. 7 and 8, are presented in the inner- and outer-scaled wall-normal coordinates and are compared with those of DNS in Figs. 9 and 10. Overall, the trends observed in Sec. III B, namely, an analogous "qualitative" behavior between DNS and the optimal QLA, are reproduced in Figs. 9 and 10 for low Reynolds numbers (up to $\mathrm{Re}_\tau = 5 \times 10^3$). By further increasing Re_τ up to $\mathrm{Re}_\tau = 10^6$, the features consistent with Townsend's attached eddy model start to appear: the wall-normal turbulence intensity and Reynolds shear stress appear to remain roughly constant [Figs. 10(d) and 10(f)], whereas the streamwise and spanwise ones exhibit an approximate logarithmic scaling [Figs. 10(b) and 10(h)]. By trial and error, the fits obtained for the present QLA at $\mathrm{Re}_\tau = 10^6$ are

$$\frac{\overline{u'u'}}{u_\tau^2} = -A_1 \ln\left(\frac{y}{h}\right) + B_1, \tag{26a}$$

$$\frac{\overline{v'v'}}{u_\tau^2} = B_2, \tag{26b}$$

$$\frac{\overline{w'w'}}{u_\tau^2} = -A_3 \ln\left(\frac{y}{h}\right) + B_3, \tag{26c}$$

where $[A_1\, A_3] = [6.5\; 0.25]$ and $[B_1\, B_2\, B_3] = [1.25\; 0.148\; –0.6]$. We shall see later that some of these constants (A_1 and B_1) should be a function of Re_τ (Fig. 12).

Despite the behaviors of the QLA qualitatively consistent with those of DNS, it should be noted that there are some differences between the QLA and DNS. First, as already discussed in

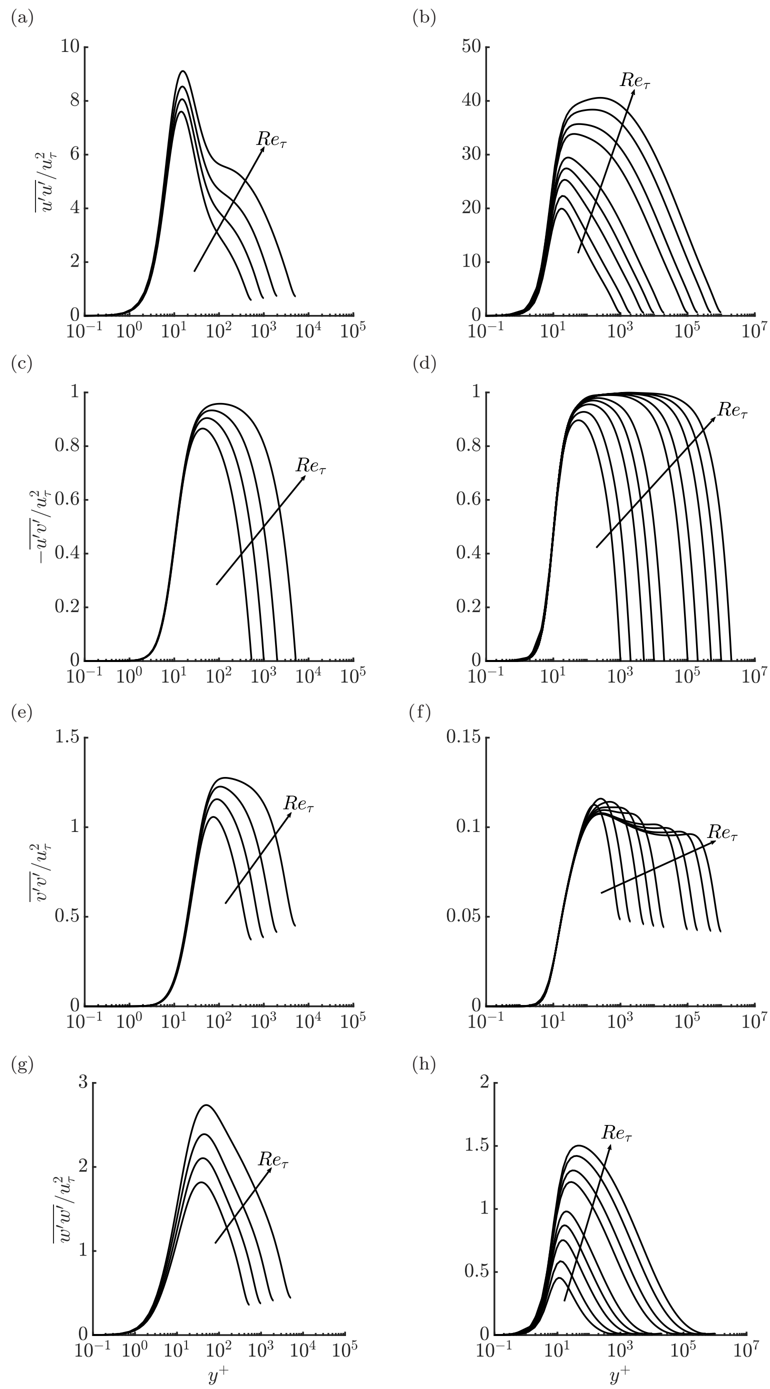

FIG. 9. Reynolds stress profiles from (a), (c), (e), (g) DNS and (b), (d), (f), (h) resolvent QLA in the inner-scaled wall-normal coordinate. Here $\mathrm{Re}_\tau = 543, 1001, 1995, 5186$ for DNS, and $\mathrm{Re}_\tau = 10^3,\ 2\times10^3,\ 5\times10^3,\ 10^4,\ 2\times10^4,\ 10^5,\ 2\times10^5,\ 5\times10^5,\ 10^6$ for QLA.

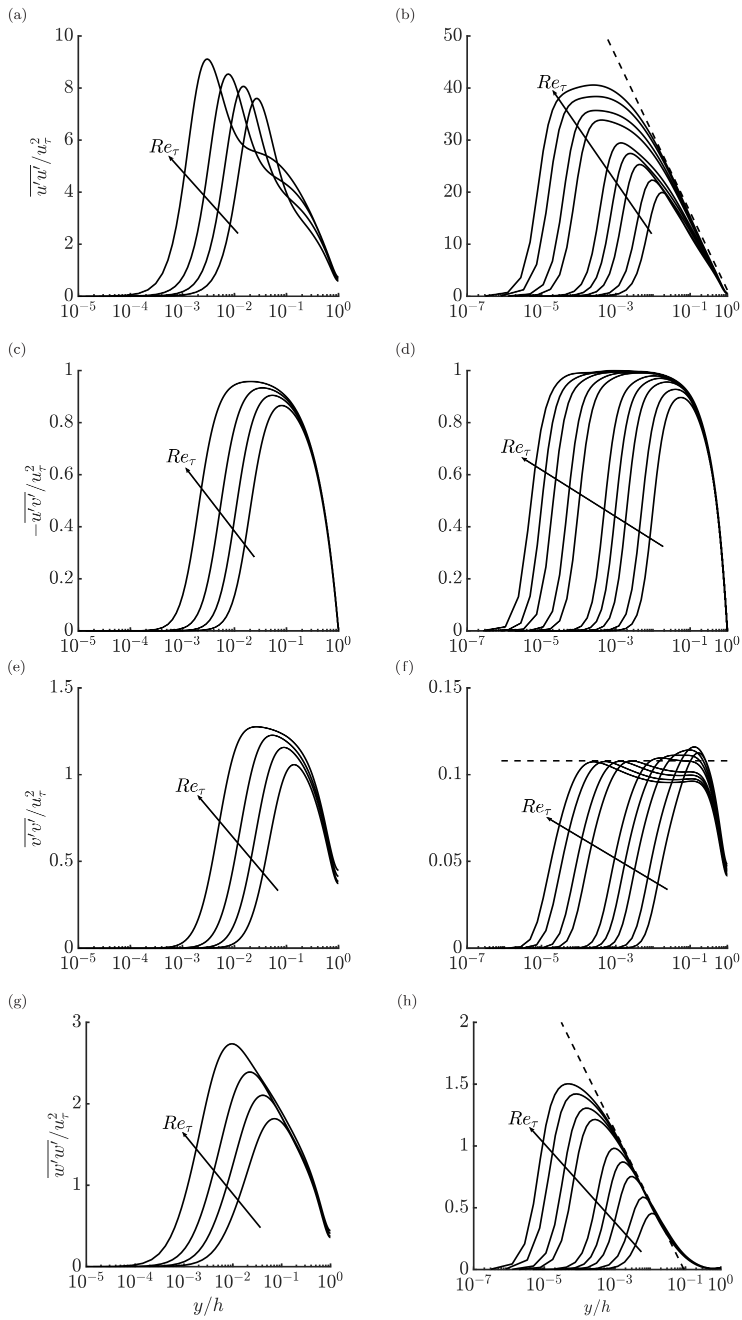

FIG. 10. Reynolds normal stress profiles from (a), (c), (e), (g) DNS and (b), (d), (f), (g) resolvent QLA in the outer-scaled wall-normal coordinate. Here $\mathrm{Re}_\tau = 543, 1001, 1995, 5186$ for DNS and $\mathrm{Re}_\tau = 10^3,\ 2\times 10^3,\ 5\times 10^3,\ 10^4,\ 2\times 10^4,\ 10^5,\ 2\times 10^5,\ 5\times 10^5,\ 10^6$ for QLA.

Sec. III B, the present QLA generates turbulence intensity highly skewed towards the streamwise component. This is due to the two-dimensional nature (in the y-z plane) of the QLA. Second, at low Reynolds numbers ($\mathrm{Re}_\tau \leqslant 5\times 10^3$), the streamwise turbulence intensity of QLA appears to be less bumpy than that of QLA, not exhibiting an evident plateau-like behavior around $y^+ = 100$ at $\mathrm{Re}_\tau \leqslant 5 \times 10^3$. However, as the Reynolds number is increased, the QLA gradually develops large intensity in the logarithmic layer (or relatively outer region). Interestingly, the wall-normal location attaining the maximum is suddenly changed from $y^+ \approx 30 - 40$ to $y^+ \approx 2000$ for $\mathrm{Re}_\tau \geqslant 5 \times 10^5$. This suggests that the QLA and DNS show similar qualitative scaling behavior, as expected from the spectra in Figs. 7 and 8, but they also have a nontrivial quantitative difference. We note that this is due to the relatively weak strength of the near-wall peak developed in the spectra of the QLA—indeed, the QLA exhibits its global maximum at $\lambda_z/h \approx 1$, whereas the DNS shows its global maximum at $\lambda_z^+ \approx 100$–200, causing its near-wall turbulence intensity relatively more pronounced than that of the QLA. Finally, the wall-normal turbulence intensity of the QLA in the near-wall and in the outer regions appears to retain an overshoot on increasing Reynolds numbers, which is not observed in that of DNS [Figs. 7(g)–7(i) and Figs. 8(e), 8(f)]. We note that such a behavior was not observed in the stochastic QLA [33], suggesting that this is presumably due to the nature of the resolvent modes skewed more towards the streamwise component than the POD modes from the stochastic response in Ref. [33]. It is not difficult to realize that all these differences between the QLA and DNS originate from the nature of the resolvent modes with $k_x = 0$ used for the linear superposition through Eq. (13). This implies that the present QLA could well be improved quantitatively by providing a delicate form of the modes for each k_z. However, it should be pointed out that this improvement would not change the basic scaling behavior of the present QLA, since the resolvent modes used for each k_z exhibit the scaling behaviors qualitatively consistent those of the Fourier modes from DNS for each k_z [22,26]. Therefore, from now on, we shall focus on studying the scaling behavior of the QLA with the Reynolds number.

Now we examine the scaling of the near-wall turbulence intensity. If the early attached eddy model [2–4,34,35] is simply extended to the near-wall region like in Ref. [40], it may be shown that the streamwise turbulence intensity at a fixed inner-scaled wall-normal location in the near-wall region is given by

$$\frac{\overline{u'u'}(y^+)}{u_\tau^2} = C_1 \ln \mathrm{Re}_\tau + C_2, \tag{27}$$

where C_1 and C_2 are constants. A considerable amount of evidence supporting (27) has been presented at least for $\mathrm{Re}_\tau \lesssim 10^4$ [51,77], although the recent experimental measurements in the CICLoPE facility up to $\mathrm{Re}_\tau = 4 \times 10^4$ [38] suggested that the near-wall peak intensity may begin to deviate from Eq. (27) for $\mathrm{Re}_\tau \gtrsim 10^4$. We note that the inner-scaled wall-normal location of the peak near-wall streamwise turbulence intensity was originally understood not to be changed with the Reynolds number, thus Eq. (27) has also been used for scaling of the peak near-wall streamwise turbulence intensity. However, more precise examinations of experimental and DNS data have revealed that the peak wall-normal location in the near-wall region slowly changes with the Reynolds number [10,33,38]. Given the wide range of the Reynolds numbers considered in this study, such a change in the peak wall-normal location would not be negligible. Therefore, Eq. (27) needs to be examined at a fixed inner-scaled wall-normal location in the near-wall region.

The other scaling that will be examined in the present study was proposed in Ref. [39], in which an asymptotic analysis of the mean streamwise momentum equation for the turbulent boundary layer is performed using DNS data. In that analysis, the streamwise near-wall turbulence intensity is given by

$$\frac{\overline{u'u'}(y^+)}{u_\tau^2} = D_1(y^+) - \frac{u_\tau}{U_{cl}} D_2(y^+) + O\left(\frac{u_\tau^2}{U_{cl}^2}\right), \tag{28}$$

where $D_1(y)$ and $D_2(y)$ are positive y-dependent functions, and U_{cl} is the outer velocity scale, i.e., the free-stream velocity for turbulent boundary layer and centreline velocity for channel flow. Here it should be mentioned that the asymptotic analysis for turbulent boundary layer in Ref. [39] may not be straightforwardly extended to internal parallel shear flows such as channel flow due to the

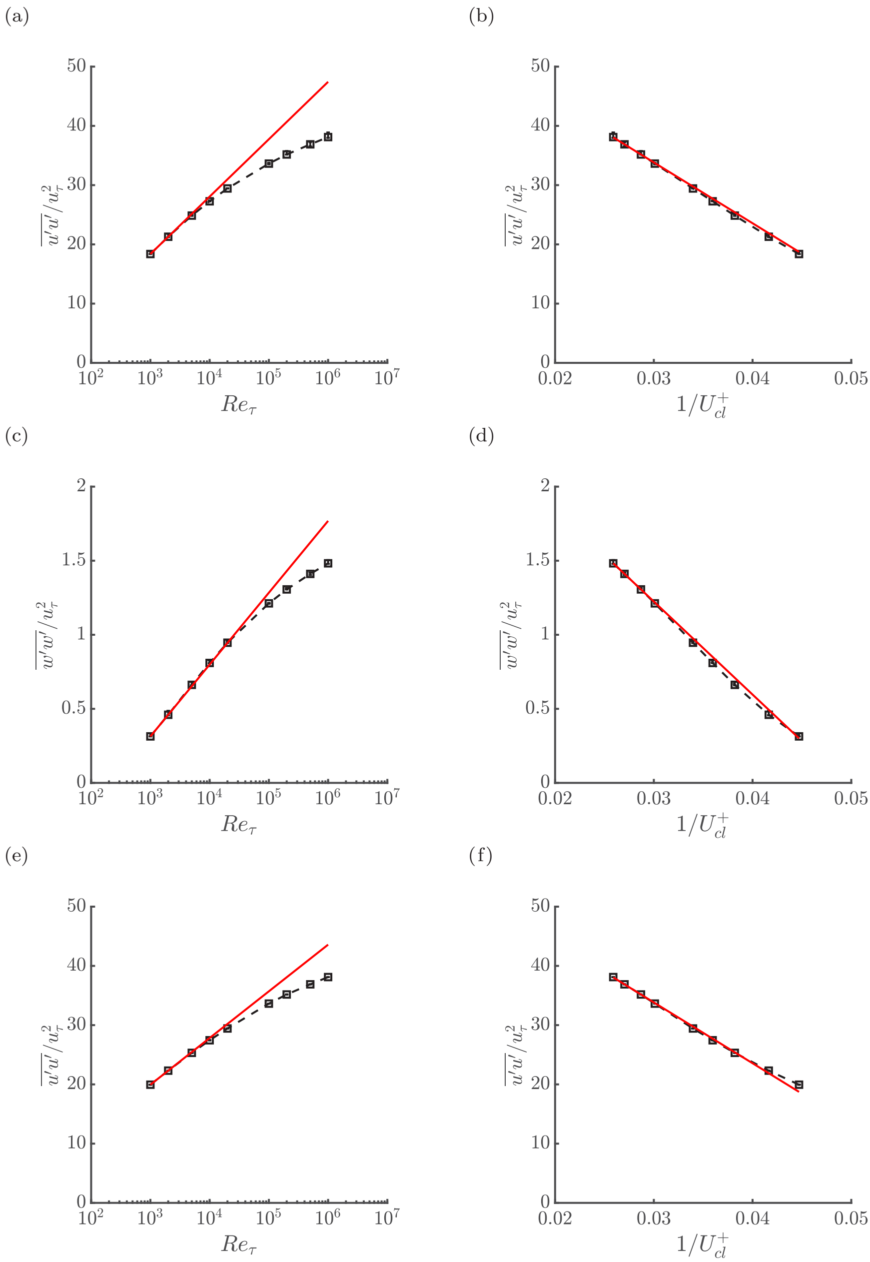

FIG. 11. Growth of the near-wall streamwise turbulence intensity ($y^+ = 30$) with (a) $\ln \mathrm{Re}_\tau$ (b) $1/U_{cl}^+$ where U_{cl}^+ denotes the mean centreline velocity. In panels (a) and (c), the red straight lines indicate a fit in the form of $\overline{u'u'}/u_\tau^2 = a_1 + b_1 \ln(\mathrm{Re}_\tau)$ where constants a_1 and b_1 are obtained from the data at $\mathrm{Re}_\tau = 1 \times 10^3$, 2×10^3. In panels (b) and (d) the red straight lines indicate a fit in the form of $\overline{u'u'}/u_\tau^2 = a_2 + b_2/U_{cl}^+$ where constants a_2 and b_2 are obtained from the data at $\mathrm{Re}_\tau = 5 \times 10^5$, 2×10^5. In panels (e) and (f) the near-wall streamwise turbulence intensity is investigated at $y^+ = y^+_{\max}$, where $y^+_{\max}$ represents the wall-normal location of the peak streamwise turbulent intensity, for $1 \times 10^3 \leqslant \mathrm{Re}_\tau \leqslant 2 \times 10^4$ and $y^+ = 30$ for $1 \times 10^5 \leqslant \mathrm{Re}_\tau \leqslant 1 \times 10^6$ in order to account for the emergence of the outer peak at large Re_τ.

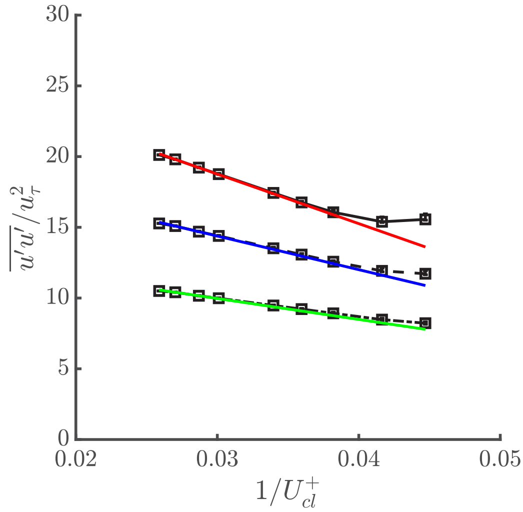

FIG. 12. Behavior of streamwise turbulence intensity in the log-layer for $y/h = 0.05$ (—), $y/h = 0.1$ (— — —), and $y/h = 0.2$ (· - ·). The colored lines represent linear fits given in the form of $\overline{u'u'}/u_\tau^2 = a_2 + b_2/U_{cl}^+$ where constants a_2 and b_2 are obtained from the data at $\mathrm{Re}_\tau = 5 \times 10^5,\ 2 \times 10^5$.

difference in the mean streamwise momentum equation between the boundary layer and channel: indeed, the mean streamwise momentum equation of channel flow does not contain any information on the streamwise turbulence intensity. However, Eq. (28) is the only Navier-Stokes-based analysis available, whereas Eq. (27) is still from a phenomenological model constructed with inviscid flow assumption.

Figure 11 shows the examination of the two scaling laws in Eqs. (27) and (28) using the streamwise and spanwise turbulence intensities from the present QLA at $y^+ = 30$ and using the near-wall peak streamwise turbulence intensity. The near-wall turbulence intensities of both streamwise and spanwise velocity components appear to follow Eq. (27) at least for $\mathrm{Re}_\tau \lesssim 10^4$ [Figs. 11(a), 11(c), 11(e)] like many previous experimental and DNS data at relatively low Reynolds numbers. However, it becomes evident that both of the streamwise and spanwise near-wall turbulence intensities deviate from Eq. (27) for $\mathrm{Re}_\tau \gtrsim 10^4$ [Figs. 11(a), 11(c), 11(e)], as was reported by the experimental data from CICLoPE facility [38]. Importantly, these near-wall intensities very closely follow Eq. (28), and they become more accurate as $\mathrm{Re}_\tau \to \infty$ ($U_{cl}^+ \to \infty$) [Figs. 11(b), 11(d), 11(f)], indicating that the two independent Navier-Stokes-based analyses (i.e., Ref. [39] and the present QLA) show a consistent behavior. Finally, it should be noted that the scaling of Eq. (27), which has been shown to depict the scaling behavior for $\mathrm{Re}_\tau \lesssim 10^4$, may well be obtained from Eq. (28). Indeed, since $U_{cl}^+ \sim \ln \mathrm{Re}_\tau$ from the log-law for the mean velocity, employing a Taylor expansion to Eq. (28) in terms of $\ln \mathrm{Re}_\tau$ about a reference Reynolds number yields

$$\frac{\overline{u'u'}(y^+)}{u_\tau^2} = C_1 + C_2 \ln \mathrm{Re}_\tau + O((\ln \mathrm{Re}_\tau)^2), \tag{29}$$

consistent with Eq. (27) at $O(\ln \mathrm{Re}_\tau)$. Further to this, Fig. 11 shows that Eq. (29) would remain a good approximation at least for a decade of Re_τ from any reference Reynolds number, suggesting that measurements and/or simulations are required to cover at least over two decades of Re_τ to correctly see the scaling behavior described by Eq. (28).

Finally, it should be mentioned that the scaling in Eq. (28) is not the only feature of the present QLA consistent with Ref. [39]. Its asymptotic analysis result also indicated that, in the overlap region (or the conventional logarithmic layer), the streamwise turbulence intensity would be proportional to $1/U_{cl}^+$, as $\mathrm{Re}_\tau \to \infty$. This result is also examined around the upper edge of

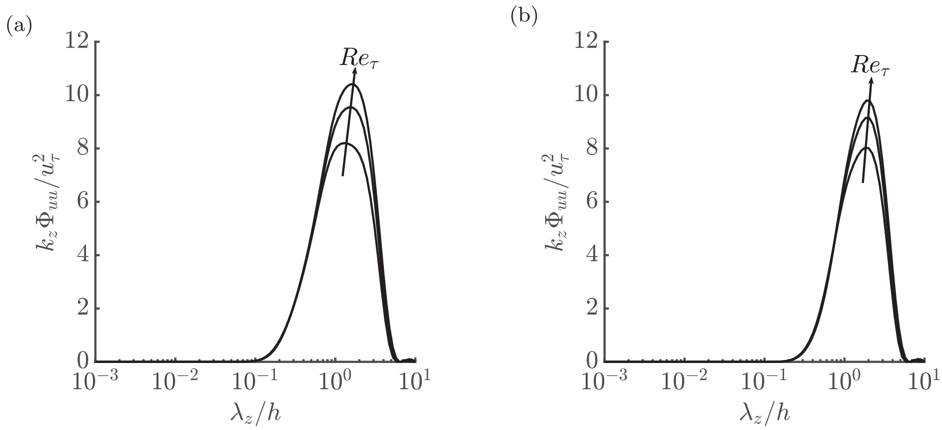

FIG. 13. Premultiplied spanwise wave number spectra of streamwise velocity at (a) $y/h = 0.05$ and (b) $y/h = 0.1$ for $\mathrm{Re}_\tau = 10^4, 10^5, 10^6$.

logarithmic layer ($y/h = 0.05, 0.1, 0.2$), as shown in Fig. 12. It is found that the streamwise turbulence intensity in those locations is indeed proportional to $1/U_{cl}^+$ as $\mathrm{Re}_\tau \to \infty$, giving credence to the asymptotic predictions in Ref. [39]. The premultiplied spectra in these locations, shown in Fig. 13, further suggest that the gradual increase of the streamwise turbulence intensity with the Reynolds number is associated with the elevation of the power spectral density at large scale (i.e., $\lambda_z/h \approx 1$), the behavior observed from the experimental and DNS data at lower Reynolds numbers: see, e.g., Refs. [10,78]. It would be interesting how such a behavior in the spectra would lead to the scaling in Eq. (28), but exploration of this issue would be beyond the scope of the present study.

C. Emergence of the outer peak in the streamwise turbulence intensity

In this subsection, the issue of how the outer part of the streamwise turbulence intensity becomes more energetic than the near-wall counter part is finally examined [Fig. 10(b)]. While it is evident that the peak wall-normal location of the streamwise turbulence intensity abruptly changes between $\mathrm{Re}_\tau = 10^5$ and $\mathrm{Re}_\tau = 10^6$ [see Fig. 7(c)], the not very well pronounced nature of the newly emerged peak makes it difficult to characterize how it would scale with Reynolds number. Therefore, here we instead explore how the near-wall turbulence intensity deviates from $\ln \mathrm{Re}_\tau$, as this would enable us to understand how the near-wall turbulence intensity gradually weakens compared to the outer counterpart.

Let us first start by assuming that the spectrum-based attached eddy model in Ref. [4] is extendable to the near-wall region by replacing its y-scaling part of the spectrum with a δ_ν-scaling one. For $\lambda_z/h \approx O(1)$, the spectra are then expected to scale well in outer units by assuming that inactive motions reach all the way down to the near-wall region:

$$\frac{k_z\Phi_{uu}(k_z, y^+)}{u_\tau^2} = g_1(k_z\delta). \tag{30a}$$

On the other hand, for $\lambda_z^+ \approx O(10^2)$ [$k_z^+ \sim O(10^{-2})$], the replacement of the y scaling in Ref. [4] with δ_ν scaling leads to an inner-scale spectrum:

$$\frac{k_z\Phi_{uu}(k_z, y^+)}{u_\tau^2} = g_2(k_z\delta_\nu). \tag{30b}$$

We now apply exactly the same procedure in Ref. [4] to Eqs. (30a) and (30b) (i.e., matching between them) for $O(\delta_\nu) \ll \lambda_z \ll O(h)$. This then leads to a k_z^{-1} spectrum, resulting in the following form

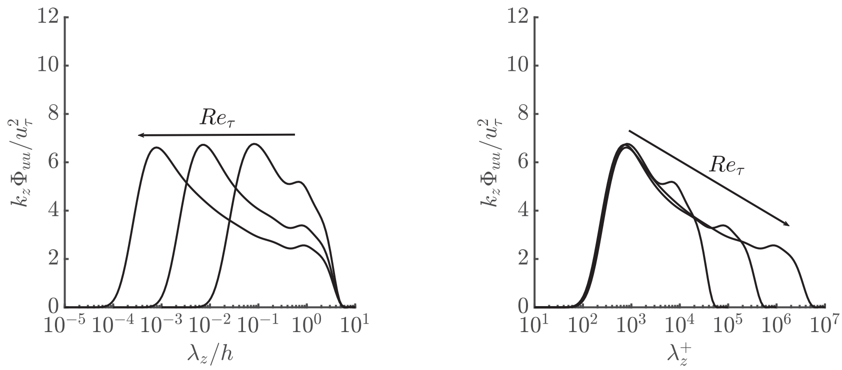

FIG. 14. Premultiplied spanwise wave number spectra of streamwise velocity at $y^+ = 30$ for $\mathrm{Re}_\tau = 10^4, 10^5, 10^6$.

of near-wall turbulence intensity at an inner-normalized location:

$$\frac{\overline{u'u'}(y^+)}{u_\tau^2} = C_1 \ln \mathrm{Re}_\tau + C_2, \tag{31}$$

where C_1 and C_2 are equivalent to those in Eq. (27).

The Reynolds number scaling in Eq. (31) is based on a simple extension of Ref. [4] to the near-wall region, and its key assumption is that the contribution of inactive motions in the near-wall region is strong enough for Eq. (30a) to be true. Let us now examine the two scalings in Eqs. (30a) and (30b). Figure 14 shows the premultiplied spanwise wave number spectra of the streamwise velocity of the present QLA in the near-wall region ($y^+ = 30$) at three different Reynolds numbers ($\mathrm{Re}_\tau = 10^4, 10^5, 10^6$). It is evident that the near-wall spectra of the streamwise velocity scale in inner units for $\lambda_z^+ \approx O(10^2)$, indicating that Eq. (30b) is a valid scaling law for the spectra obtained from the present QLA. On the other hand, the outer scaling given in Eq. (30a) does not appear to be valid because the spectra at $\lambda_z \sim O(h)$ do not scale in the outer unit—indeed, there is no reason for Eq. (30a) to be valid in the near-wall region where the viscous inner length scale δ_ν is supposed to be important. Consistent with this, the intensity of the spectrum at $\lambda_z \sim O(h)$ is weakened as Re_τ is increased, suggesting that the extent of the large-scale inactive motion penetrating in the near-wall region is gradually decreasing with Re_τ. This behavior also appears to prevent the formation of a well-developed k_z^{-1} spectrum over a wide range of λ_z. Last, the spectra in Fig. 14 indicate that, at low Reynolds numbers, the scale interactions in the near-wall region is rather directly between the inner- and outer-scaling motions due to the little length-scale separation between two [see also the recent review [79] on this issue]. However, as the Reynolds number increases, the near-wall spectra are contributed by the wall-reach motions at the length scale of $O(\delta_\nu) < \lambda_z < O(h)$ with large separation between the inner and outer length scales. This implies that the scale interactions in the near-wall region takes place across the entire length scales at high Reynolds numbers, while the direct interaction between the inner and outer scales becomes weaker on increasing the Reynolds number due to the weakened outer-scaled spectra. This observation is also consistent with the wall-reaching nature of inactive motions of the y-scaling attached eddies reported in Refs. [15,26,59,80].

It is evident that all these behaviors are due to the viscous effect cased by the no-slip boundary condition on the large-scale inactive motion, the near-wall scaling behavior of which was discussed in detail in Ref. [16]. Furthermore, since the near-wall spectrum at $\lambda_z \sim O(h)$ becomes weaker with Re_τ, the near-wall turbulence intensity would gradually deviate from Eq. (31), consistent with the observations made in Fig. 11. This also implies that, in the logarithmic region where the viscous effect is not expected to be strong, the intensity of the outer-scaling spectrum would not be weakened with increasing Re_τ. In fact, Fig. 13 suggests that it becomes stronger instead, explaining why the streamwise turbulence intensity exhibits a sudden change in its peak location with increasing

Re_τ. Finally, the emergence of the peak streamwise turbulence intensity in the logarithmic layer at $\mathrm{Re}_\tau \gtrsim 5 \times 10^5$ in the QLA data suggests that the same may happen in experimental and DNS data, if they become available in the future. We note that this Reynolds number predicted by the present QLA is two or three order of magnitude lower than $\mathrm{Re}_\tau \approx O(10^8)$ estimated in Ref. [77], where the prediction is made by carefully extrapolating their experimental data at $\mathrm{Re}_\tau \lesssim O(10^4)$. Here it should be pointed that their prediction of the Reynolds number being $\mathrm{Re}_\tau \approx O(10^8)$ is based on $\ln \mathrm{Re}_\tau$ scaling in Eq. (27) for the near-wall turbulence intensity. However, if the near-wall streamwise turbulence intensity is lower than the one from Eq. (27) for $\mathrm{Re}_\tau \gtrsim O(10^4)$, it may well be possible that the Reynolds number, at which the outer peak takes over the near-wall one, would be lower than $\mathrm{Re}_\tau \sim O(10^8)$, consistent with the prediction of the present QLA.

V. CONCLUDING REMARKS

In this study, the quasilinear approximation, developed in Ref. [33] with a stochastic forcing and POD modes, has been extended by employing the resolvent analysis framework. The flow is decomposed into a mean and fluctuations using the Reynolds decomposition. For the mean, all the nonlinearites are kept, whereas, for the fluctuations, the equations are linearized around the mean and the self-interacting nonlinearities are modeled using an eddy-viscosity-based diffusion and a stochastic forcing. The resolvent modes are subsequently utilized to characterize the fluctuations in response to the stochastic forcing. Their amplitudes are self-consistently determined by solving an optimization problem, which minimizes the difference between the Reynolds shear stresses from the mean and fluctuation equations, subject to the constraint that the forcing must be sufficiently smooth in Fourier space.

For the purpose of reducing computational cost towards an extremely high Reynolds number relevant to atmospheric surface layer ($\mathrm{Re}_\tau = 10^6$), the proposed resolvent QLA is carefully approximated further. This enables us to construct the QLA using two leading resolvent modes of the Fourier components of $k_x = 0$ and $\omega = 0$ (i.e. QLA with optimal forcing). Although this choice of the modes does not make the QLA lose its basic scaling behavior, it should be mentioned that it is essentially *ad hoc* and undermines the accuracy of the QLA together with its nonunique nature, requiring further improvement in the future.

Application of the QLA to a turbulent channel flow up to $\mathrm{Re}_\tau = 10^6$ reveals several notable statistical features. They would potentially be useful for the interpretations of experimental and DNS data at extremely high Reynolds numbers, when they become available:

(1) Any visibly well-developed inverse-law power spectra are not observed even at $\mathrm{Re}_\tau = 10^6$. The QLA data suggest that a significant potion of the lower part of the logarithmic layer (or mesolayer) is under the influence of viscous force originating from the wall. The spectra at the outer length scale in this region exhibit a nontrivial difference from the outer-scaling law proposed in the early spectrum-based attached eddy model [4].

(2) The near-wall streamwise and spanwise turbulence intensities of the proposed QLA are found to deviate from the $\ln \mathrm{Re}_\tau$ for $\mathrm{Re}_\tau \gtrsim O(10^4)$, while exhibiting a scaling proportional to $1/U_{cl}^+$. The QLA data suggest that the streamwise turbulence intensity in the logarithmic region at a given outer-scaled wall-normal location is also proportional to $1/U_{cl}^+$. These scaling behaviors consistently follow those proposed in Ref. [39], where the streamwise turbulence intensities in both the near-wall and outer regions were shown to be proportional to $1/U_{cl}^+$ using an asymptotic analysis of the Navier-Stokes equations with DNS data.

(3) The QLA data revealed that the streamwise turbulence intensity in the logarithmic layer can become greater than the near-wall counterpart at $\mathrm{Re}_\tau \sim O(10^5)$. This is due to the gradually weakening near-wall spectra at large scale with increasing Re_τ, suggesting that the influence of viscous force on the wall-reaching large-scale inactive motions would be the origin of this behavior.

It appears that the scaling behaviors gained in the present QLA are not consistent with those proposed based on the early attached eddy models. However, it should be pointed out that the present QLA can be viewed as an improved version of such attached eddy models, because it retains exactly

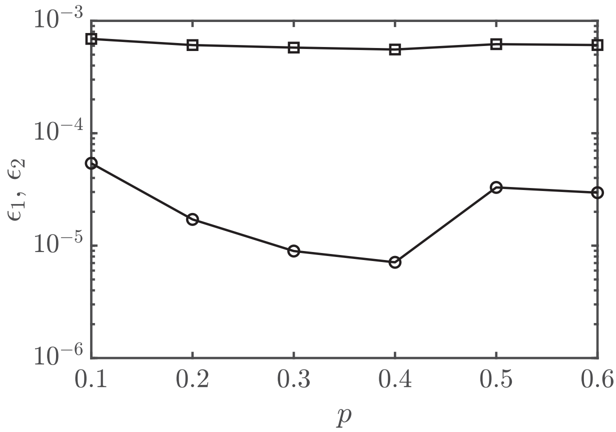

FIG. 15. Sensitivity to the optimization parameter, p, used in order to mitigate the sharp decay in k_z of the singular values of the resolvent operator. Here ϵ_1 ($\square$) refers to the Q-norm error, $\|\overline{u'v'} - \langle u'v'\rangle\|_Q$ defined in Sec. II B and ϵ_2 ($\circ$) denotes the standard $\mathcal{L}_2$-norm error.

the same mathematical structure with them: i.e., linear superposition of self-similar statistical structures/modes subject to the given Reynolds shear stress. Indeed, the stationary resolvent modes for $k_x = 0$ in this study and the time-domain POD modes in Ref. [33] were both analytically and numerically shown to be approximately self-similar with y for $O(100\delta_\nu) < \lambda_z < O(h)$ due to the logarithmic mean velocity (see Fig. 4 in Ref. [22]). From this viewpoint, the primary differences of the present QLA from the early attached models are the following: (1) the no-slip boundary condition is implemented to the individual self-similar statistical structures and (2) the full Reynolds shear stress profile is considered using the empirical model in Ref. [41]. Therefore, in principle, the present QLA is supposed to reproduce the result of the early attached eddy model in the limit of $\mathrm{Re}_\tau \to \infty$, if the resolvent modes used in this study are redesigned to satisfy a slip boundary condition consistent with the original model of Townsend [1]. This is also the fundamental reason why the streamwise and spanwise turbulence intensities of the present QLA exhibit logarithmic wall-normal dependencies, while the wall-normal intensity and the Reynolds shear stress remain constant at least in an approximate manner (see Fig. 10). Therefore, the results in the present QLA do not indicate any issue in the basic modeling idea of the attached eddy models, but the potential limitations caused by the inviscid flow assumptions in the early attached eddy models. If these assumptions are carefully removed by utilizing the Navier-Stokes equations, the viscous version of the attached eddy model (i.e., the present QLA) shows consistent behaviors with the other Navier-Stokes-based asymptotic analysis in Ref. [39]. It is therefore hoped that the qualitative scaling behaviors proposed by the present QLA would be useful when new experimental and DNS data emerge at higher Reynolds numbers.

ACKNOWLEDGMENTS

Y.H. thanks Prof. P. A. Monkewitz and Prof. H. Nagib for sharing very helpful discussions about their previous work [39]. Y.H. gratefully acknowledges the financial support from the Leverhulme trust (RPG-2019-123) and the Engineering Physical Science Research Council (EPSRC; EP/T009365/1) in the United Kingdom.

APPENDIX A: SENSITIVITY TO OPTIMIZATION PARAMETER *p*

In this Appendix, a sensitivity analysis is performed on the optimization parameter, p, that is introduced to mitigate the sharp decay of singular values of the resolvent operator [see Eq. (15)]. In Fig. 15 it can be seen that as p is increased the Q-norm error remains almost constant. On the error

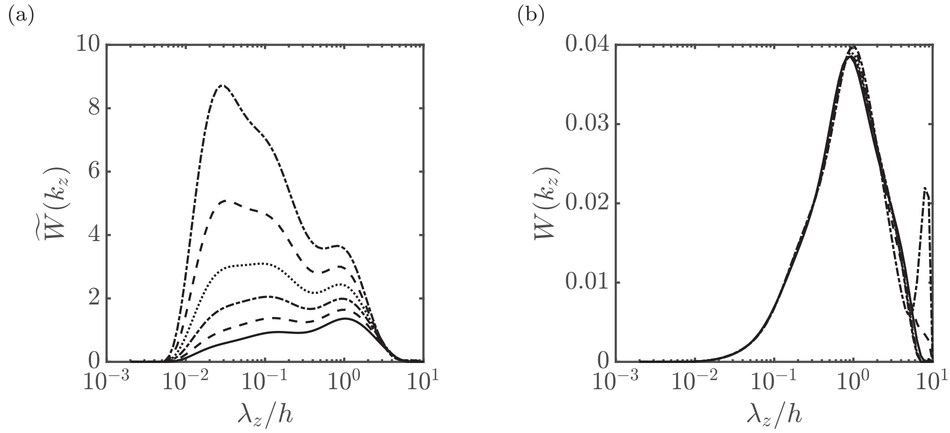

FIG. 16. Sensitivity of the modified and original weight functions, defined in Eq. (16), as p is varied. Here $p = 0.1$ (—), $p = 0.2$ (− − −), $p = 0.3$ (· - ·), $p = 0.4$ (· · ·), $p = 0.5$ (− − −), $p = 0.6$ (· - ·).

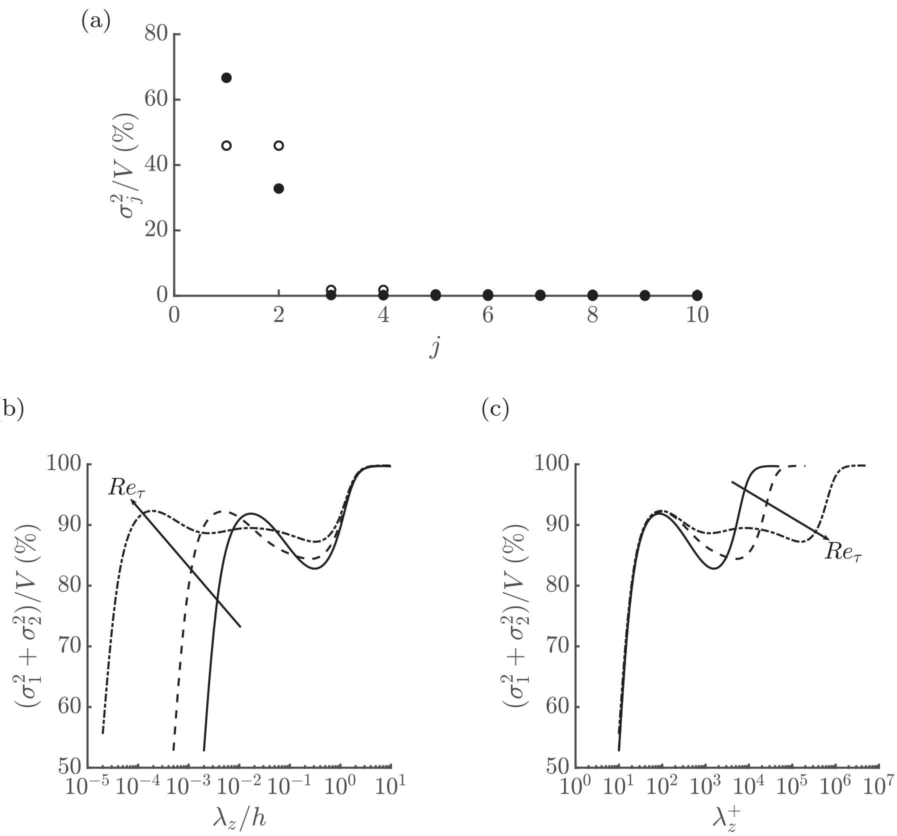

FIG. 17. Energy contents of the resolvent modes for $k_x = 0$ and $\omega = 0$: (a) the contribution of the first 10 modes (σ_j^2/V) to the energy of all modes ($V = \sum_{\forall j} \sigma_j^2$) for $\lambda_z = 3.5h$ (•) and $\lambda_z^+ = 80$ (○) at $\mathrm{Re}_\tau = 5 \times 10^3$. In panels (b) and (c) the contribution of the two most energetic modes is investigated over (b) the outer- and (c) inner-scaled spanwise wavelengths for $\mathrm{Re}_\tau = 5 \times 10^3$ (—), $\mathrm{Re}_\tau = 2 \times 10^4$ (− − −), and $\mathrm{Re}_\tau = 5 \times 10^5$ (· - ·).

hand, the $\mathcal{L}_2$ norm error experiencesa nontrivial drop for $p = 0.4$. It is also instructive to check the behavior of the weight functions as p is varied (Fig 16). In general the smoothness of the modified weight function [Fig. 2(a)] deteriorates as p is increased. This can also be verified in Fig. 2(b), where the original weight function exhibits a second odd peak near $\lambda_z \approx 10h$. For these reasons, the value of p which provides the smallest optimization error and adequate smoothness is chosen to be $p = 0.4$.

APPENDIX B: ENERGY CONTENTS OF LEADING RESOLVENT MODES

Here we report how much energy is contained in the two leading resolvent modes. Figure 17(a) shows the contribution of first 10 modes to the energy of all modes for the streamwise uniform ($k_x = 0$) and stationary ($\omega = 0$) case. It is seen that the leading two modes contain most of the energy. Examination of their contribution at different λ_z and Re_τ shows that the leading two resolvent modes consistently contribute more than 80% to the total energy for $50\delta_\nu \leqslant \lambda_z \leqslant 10h$ [Figs. 17(b) and 17(c)].

---

[1] A. A. Townsend, *The Structure of Turbulent Shear Flow*, 1st ed. (Cambridge University Press, Cambridge, 1956).

[2] A. A. Townsend, *The Structure of Turbulent Shear Flow*, 2nd ed. (Cambridge University Press, Cambridge, 1976).

[3] A. E. Perry and M. S. Chong, On the mechanism of turbulence, J. Fluid Mech. **119**, 173 (1982).

[4] A. E. Perry, S. Henbest, and M. S. Chong, A theoretical and experimental study of wall turbulence, J. Fluid Mech. **165**, 163 (1986).

[5] I. Marusic and J. P. Monty, Attached eddy model of wall turbulence, Annu. Rev. Fluid Mech. **51**, 49 (2019).

[6] Y. Hwang and M. Lee, The mean logarithm emerges with self-similar energy balance, J. Fluid Mech. **903**, R6 (2020).

[7] J. Jiménez and S. Hoyas, Turbulent fluctuations above the buffer layer of wall-bounded flows, J. Fluid Mech. **611**, 215 (2008).

[8] M. Hultmark, M. Vallikivi, S. C. C. Bailey, and A. J. Smits, Turbulent Pipe Flow at Extreme Reynolds Numbers, Phys. Rev. Lett. **108**, 094501 (2012).

[9] I. Marusic, J. P. Monty, M. Hultmark, and A. J. Smits, On the logarithmic region in wall turbulence, J. Fluid Mech. **716**, R3 (2013).

[10] M. K. Lee and R. D. Moser, Direct numerical simulation of turbulent channel flow up to $\mathrm{Re}_\tau \approx 5200$, J. Fluid Mech. **774**, 395 (2015).

[11] W. J. Baars and I. Marusic, Data-driven decomposition of the streamwise turbulence kinetic energy in boundary layers. Part 2: Integrated energy and A_1, J. Fluid Mech. **882**, A26 (2020).

[12] J. C. del Álamo, J. Jiménez, P. Zandonade, and R. D. Moser, Self-similar vortex clusters in the turbulent logarithmic region, J. Fluid Mech. **561**, 329 (2006).

[13] Y. Hwang and C. Cossu, Self-sustained processes in the logarithmic layer of turbulent channel flows, Phys. Fluid **23**, 061702 (2011).

[14] A. Lozano-Durán and J. Jiménez, Time-resolved evolution of coherent structures in turbulent channels: Characterization of eddies and cascades, J. Fluid Mech. **759**, 432 (2014).

[15] Y. Hwang, Statistical structure of self-sustaining attached eddies in turbulent channel flow, J. Fluid Mech. **723**, 264 (2015).

[16] Y. Hwang and Y. Bengana, Self-sustaining process of minimal attached eddies in turbulent channel flow, J. Fluid Mech. **795**, 708 (2016).

[17] L. H. O. Hellstöm, I. Marusic, and A. J. Smits, Self-similarity of the large-scale motions in turbulent pipe flow, J. Fluid Mech. **792**, R1 (2016).

[18] J. Hwang and H. J. Sung, Wall-attached structures of velocity fluctuations in a turbulent boundary layer, J. Fluid Mech. **856**, 958 (2018).
[19] C. Cheng, W. Li, A. Lozano-Durán, and H. Liu, Identity of attached eddies in turbulent channel flows with bidimensional empirical mode decomposition, J. Fluid Mech. **870**, 1037 (2019).
[20] W. J. Baars and I. Marusic, Data-driven decomposition of the streamwise turbulence kinetic energy in boundary layers. Part 1: Energy spectra, J. Fluid Mech. **882**, A25 (2020).
[21] J. C. del Álamo and J. Jiménez, Linear energy amplification in turbulent channels., J. Fluid Mech. **559**, 205 (2006).
[22] Y. Hwang and C. Cossu, Linear non-normal energy amplification of harmonic and stochastic forcing in the turbulent channel flow, J. Fluid Mech. **664**, 51 (2010).
[23] J. C. Klewicki, Self-similar mean dynamics in turbulent wall flows, J. Fluid Mech. **718**, 596 (2013).
[24] R. Moarref, A. S. Sharma, J. A. Tropp, and B. J. McKeon, Model-based scaling of the streamwise energy density in high-Reynolds-number turbulent channels, J. Fluid Mech. **734**, 275 (2013).
[25] Y. Hwang, A. P. Willis, and C. Cossu, Invariant solutions of minimal large-scale structures in turbulent channel flow for Re_τ up to 1000, J. Fluid Mech. **802**, R1 (2016).
[26] Y. Hwang, Mesolayer of attached eddies in turbulent channel flow, Phys. Rev. Fluids **1**, 064401 (2016).
[27] C. Cossu and Y. Hwang, Self-sustaining process at all scales in wall-bounded turbulent shear flows, Phil. Trans. R. Soc. A **375**, 20160088 (2017).
[28] B. Eckhardt and S. Zammert, Small scale exact coherent structures at large Reynolds numbers in plane Couette flow, Nonlinearity **31**, R66 (2018).
[29] S. B. Vadarevu, S. Symon, S. J. Illingworth, and I. Marusic, Coherent structures in the linearized impulse response of turbulent channel flow, J. Fluid Mech. **863**, 1190 (2019).
[30] B. J. McKeon, Self-similar hierarchies and attached eddies, Phys. Rev. Fluids **4**, 082601(R) (2019).
[31] Q. Yang, A. P. Willis, and Y. Hwang, Exact coherent states of attached eddies in channel flow, J. Fluid Mech. **862**, 1029 (2019).
[32] P. Doohan, A. P. Willis, and Y. Hwang, Shear stress-driven flow: The state space of near-wall turbulence as $\mathrm{Re}_\tau \to \infty$, J. Fluid Mech. **874**, 606 (2019).
[33] Y. Hwang and B. E. Eckhardt, Attached eddy model revisited using a minimal quasilinear approximation, J. Fluid Mech. **894**, A23 (2020).
[34] A. E. Perry and I. Marusic, A wall-wake model for the turbulence structure of boundary layers. Part 1. Extension of the attached eddy hypothesis, J. Fluid Mech. **298**, 361 (1995).
[35] I. Marusic and A. E. Perry, A wall-wake model for the turbulence structure of boundary layers. Part 2. Further experimental support, J. Fluid Mech. **298**, 389 (1995).
[36] N. Afzal, Fully developed turbulent flow in a pipe: An intermediate layer, Ing.-Arch. **52**, 355 (1982).
[37] T. Wei, P. Fife, J. C. Klewicki, and P. McMurtry, Properties of the mean momentum balance in turbulent boundary layer, pipe and channel flows., J. Fluid Mech. **522**, 303 (2005).
[38] C. E. Willert, J. Soria, M. Stanislas, J. Klinner, O. Amili, M. Eisfelder, C. Cuvier, G. Bellani, T. Fiorini, and A. Talamelli, Near-wall statistics of a turbulent pipe flow at shear Reynolds numbers up to 40 000, J. Fluid Mech. **826**, R5 (2017).
[39] P. A. Monkewitz and H. M. Nagib, Large-Reynolds-number asymptotics of the streamwise normal stress in zero-pressure-gradient turbulent boundary layers, J. Fluid Mech. **783**, 474 (2015); P. Monkewitz and H. Nagib (private communication).
[40] I. Marusic and G. J. Kunkel, Streamwise turbulent intensity formulation for flat-plate boundary layers, Phys. Fluids **15**, 2461 (2003).
[41] R. D. Cess, A survey of the literature on heat transfer in turbulent tube flow, Research Report 8–0529–R24, Westinghouse (1958).
[42] M. R. Jovanović and B. Bamieh, Modelling flow statistics using the linearized Navier-Stokes equations, in *Proceedings of the 40th IEEE Conference on Decision and Control* (Orlando, FL, 2001), pp. 4944–4949.
[43] R. Moarref, M. R. Jovanovic, J. A. Tropp, A. S. Sharma, and B. J. McKeon, A low-order decomposition of turbulent channel flow via resolvent analysis and convex optimization, Phys. Fluids **26**, 051701 (2014).
[44] A. Zare, M. R. Jovanović, and T. Georgiou, Colour of turbulence, J. Fluid Mech. **812**, 636 (2017).

[45] A. Zare, T. T. Georgiou, and M. R. Jovanović, Stochastic dynamical modeling of turbulent flows, Annu. Rev. Control Robot. Auton. Syst **3**, 636 (2020).
[46] R. M. McMullen, K. Rosenberg, and B. J. McKeon, Interaction of forced Orr-Sommerfeld and Squire modes in a low-order representation of turbulent channel flow, Phys. Rev. Fluids **5**, 084607 (2020).
[47] M. R. Jovanović, From bypass transition to flow control and data-driven turbulence modeling: An input-output viewpoint, Annu. Rev. Fluid Mech. **53**, 311 (2021).
[48] Y. Hwang and C. Cossu, Amplification of coherent streaks in the turbulent Couette flow: An input-output analysis at low Reynolds number, J. Fluid Mech. **643**, 333 (2010).
[49] B. J. McKeon and A. S. Sharma, A critical-layer framework for turbulent pipe flow, J. Fluid Mech. **658**, 336 (2010).
[50] B. J. McKeon, The engine behind (wall) turbulence: Perspectives on scale interactions, J. Fluid Mech. **817**, P1 (2017).
[51] I. Marusic, B. J. McKeon, P. A. Monkewitz, H. M. Nagib, A. J. Smits, and K. R. Sreenivasan, Wall-bounded turbulent flows at high Reynolds numbers: Recent advances and key issues, Phys. Fluids **22**, 065103 (2010).
[52] K. M. Butler and B. F. Farrell, Optimal perturbations and streak spacing in wall-bounded turbulent shear flow, Phys. Fluids **5**, 774 (1993).
[53] G. Pujals, M. García-Villalba, C. Cossu, and S. Depardon, A note on optimal transient growth in turbulent channel flows, Phys. Fluids **21**, 015109 (2009).
[54] A. P. Willis, Y. Hwang, and C. Cossu, Optimally amplified large-scale streaks and drag reduction in the turbulent pipe flow, Phys. Rev. E **82**, 036321 (2010).
[55] R. Moarref and M. R. Jovanović, Model-based design of transverse wall oscillations for turbulent drag reduction, J. Fluid Mech. **707**, 205 (2012).
[56] S. J. Illingworth, J. P. Monty, and I. Marusic, Estimating large-scale structures in wall turbulence using linear models, J. Fluid Mech. **842**, 146 (2018).
[57] A. Madhusudanan, S. J. Illingworth, and I. Marusic, Coherent large-scale structures from the linearized Navier-Stokes equations, J. Fluid Mech. **873**, 89 (2019).
[58] A. Towne, A. Lozano-Durán, and X. I. A. Yang, Resolvent-based estimation of space-time flow statistics, J. Fluid Mech. **883** (2020).
[59] M. Cho, Y. Hwang, and H. Choi, Scale interactions and spectral energy transfer in turbulent channel flow, J. Fluid Mech. **854**, 474 (2018).
[60] J. M. Hamilton, J. Kim, and F. Waleffe, Regeneration mechanisms of near-wall turbulence structures, J. Fluid Mech. **287**, 317 (1995).
[61] W. Schoppa and F. Hussain, Coherent structure generation in near-wall turbulence, J. Fluid Mech. **453**, 57 (2002).
[62] J. Park, Y. Hwang, and C. Cossu, On the stability of large-scale streaks in the turbulent Couette and Poiseuille flows, C. R. Mècanique **339**, 1 (2011).
[63] A. Cassinelli, M. de Giovanetti, and Y. Hwang, Streak instability in near-wall turbulence revisited, J. Turbul. **18**, 443 (2017).
[64] M. de Giovanetti, H. J. Sung, and Y. Hwang, Streak instability in turbulent channel flow: The seeding mechanism of large-scale motions, J. Fluid Mech. **832**, 483 (2017).
[65] S. J. Kline, W. C. Reynolds, F. A. Schraub, and P. W. Runstadler, The structure of turbulent boundary layers, J. Fluid Mech. **30**, 741 (1967).
[66] J. del Álamo and J. Jiménez, Spectra of the very large anisotropic scales in turbulent channels, Phys. Fluids **15**, L41 (2003).
[67] G. Dergham, D. Sipp, and J.-C. Robinet, Stochastic dynamics and model reduction of amplifier flows: The backward facing step flow, J. Fluid. Mech. **719**, 406 (2013).
[68] J. Holford, M. K. Lee, and Y. Hwang, A three-dimensional extension of minimal quasi-linear approximation for channel flow, Bull. Am. Phys. Soc. S10.00019 (2020).
[69] J. A. C. Weideman and S. C. Reddy, A MATLAB differentiation matrix suite, ACM Trans. Math. Soft. **26**, 465 (2000).
[70] S. Boyd and L. Vandenberghe, *Convex Optimization* (Cambridge University Press, Cambridge, 2004).

[71] P. J. Schmid and D. S. Henningson, *Stability and Transition in Shear Flows* (Springer, New York, 2001).
[72] S. C. Reddy and L. N. Trefethen, Pseudospectra of the convection-diffusion operator, SIAM J. Appl. Math. **54**, 1634 (1994).
[73] B. Bamieh and M. Dahleh, Energy amplification in channel flows with stochastic excitation, Phys. Fluids **13**, 3258 (2001).
[74] M. R. Jovanović and B. Bamieh, Componentwise energy amplification in channel flow, J. Fluid Mech. **543**, 145 (2005).
[75] J. F. Morrison, W. Jiang, B. J. McKeon, and A. J. Smits, Reynolds Number Dependence of Streamwise Velocity Spectra in Turbulent Pipe Flow, Phys. Rev. Lett. **88**, 214501 (2002).
[76] J. F. Morrison, B. J. McKeon, W. Jiang, and A. J. Smits, Scaling of the streamwise velocity component in turbulent pipe flow, J. Fluid Mech. **508**, 99 (2004).
[77] M. Samie, I. Marusic, N. Hutchins, M. K. Fu, Y. Fan, M. Hultmark, and A. J. Smits, Fully resolved measurements of turbulent boundary layer flows up to $Re_\tau = 20\,000$, J. Fluid Mech. **851**, 391 (2018).
[78] N. Hutchins and I. Marusic, Evidence of very long meandering features in the logarithmic region of turbulent boundary layers, J. Fluid Mech. **579**, 1 (2007).
[79] I. Marusic, W. J. Baars, and N. Hutchins, Scaling of the streamwise turbulence intensity in the context of inner-outer interactions in wall-turbulence, Phys. Rev. Fluids **2**, 100502 (2017).
[80] R. Deshpande, J. P. Monty, and I. Marusic, Active and inactive components of the streamwise velocity in wall-bounded turbulence, J. Fluid Mech. (to be published 2020).